The Astrophysical Journal, 819:104 (17pp), 2016 March 10 doi:10.3847/0004-637X/819/2/104

ON THE ROLE OF TACHOCLINES IN SOLAR AND STELLAR DYNAMOS

G. Guerrero[1], P. K. Smolarkiewicz[2], E. M. de Gouveia Dal Pino[3], A. G. Kosovichev[4], and N. N. Mansour[5]
[1] Physics Department, Universidade Federal de Minas Gerais, Av. Antonio Carlos, 6627, Belo Horizonte, MG, 31270-901, Brazil; guerrero@fisica.ufmg.br
[2] European Centre for Medium-Range Weather Forecasts, Reading RG2 9AX, UK; smolar@ecmwf.int
[3] Astronomy Department, IAG-USP Rua do mato, 1226, São Paulo, SP, 05508-090, Brazil; dalpino@astro.iag.usp.br
[4] New Jersey Institute of Technology, Newark, NJ 07103, USA; sasha@bbso.njit.edu
[5] NASA, Ames Research Center, Moffett Field, Mountain View, CA 94040, USA; Nagi.N.Mansour@nasa.gov
Received 2015 July 15; accepted 2015 December 11; published 2016 March 3

ABSTRACT

Rotational shear layers at the boundary between radiative and convective zones, tachoclines, play a key role in the process of magnetic field generation in solar-like stars. We present two sets of global simulations of rotating turbulent convection and dynamo. The first set considers a stellar convective envelope only; the second one, aiming at the formation of a tachocline, also considers the upper part of the radiative zone. Our results indicate that the resulting properties of the mean flows and dynamo, such as the growth rate, saturation energy, and mode, depend on the Rossby number (*Ro*). For the first set of models either oscillatory (with ∼2 yr period) or steady dynamo solutions are obtained. The models in the second set naturally develop a tachocline, which in turn leads to the generation of a strong mean magnetic field. Since the field is also deposited in the stable deeper layer, its evolutionary timescale is much longer than in the models without a tachocline. Surprisingly, the magnetic field in the upper turbulent convection zone evolves on the same timescale as the deep field. These models result in either an oscillatory dynamo with a ∼30 yr period or a steady dynamo depending on *Ro*. In terms of the mean-field dynamo coefficients computed using the first-order smoothing approximation, the field evolution in the oscillatory models without a tachocline seems to be consistent with dynamo waves propagating according to the Parker–Yoshimura sign rule. In the models with tachoclines the dynamics is more complex and involves other transport mechanisms as well as tachocline instabilities.

Key words: stars: activity – stars: interiors – stars: magnetic field – Sun: interior – Sun: magnetic fields – Sun: rotation

1. INTRODUCTION

One of the most challenging questions in astrophysics is the origin of stellar magnetism. More specifically, we do not yet know where inside stars the large-scale magnetic fields are generated and sustained. The best astrophysics laboratory in which to study stellar magnetism is our host star, the Sun. Its magnetic field at photospheric levels can be observed in detail, and is depicted in the well known time–latitude "butterfly" diagram. It summarizes the cyclic properties of the surface evolution of the field, its migration patterns, the periodicity of magnetic activity, and polarity reversals. The morphology and distribution of the field in deeper layers, unfortunately, still elude any kind of observation. In other solar-like stars (in the main sequence and with spectral types from F to M) the observations of magnetic field are less detailed. Nevertheless, cyclic magnetic activity, with periods between 5 and 25 years, has been observed in a good sample of stars (Baliunas et al. 1995). In the same work, the authors also reported observations of flat, non-oscillatory, magnetic activity. A general trend is that the strength of the magnetic field increases with the rotation rate of the star. More recently, Petit et al. (2008) have been able to infer the topology of the surface magnetic field of four stars that could be classified as solar twins (with stellar parameters close to those of the Sun). Their results indicate that the toroidal field strength is proportional to the rotation rate but the poloidal component anticorrelates with it. All these observations allow us to look at stellar magnetism from a broad perspective, that can add new constraints on the underlying processes and ultimately lead to a better understanding of it.

From the theoretical point of view, the generation and evolution of large-scale magnetic fields in stars (and other cosmic objects) has been studied using the mean-field dynamo theory (see Brandenburg & Subramanian 2005, for a complete review). The mean-field induction equation implies that the dominant term generating an azimuthal (toroidal) magnetic field depends on gradients of the angular velocity, $(\overline{\boldsymbol{B}}_{\rm p}\cdot\nabla)\Omega$, where Ω is the mean angular velocity and $\overline{\boldsymbol{B}}_{\rm p}$ is a pre-existing large-scale poloidal field. The generation of the poloidal field relies on the turbulent helicities, the so-called α-effect, a non-diffusive contribution of the electromotive force whose dependence on the convective turbulence and rotation is still uncertain. Under appropriate conditions, the evolution of the magnetic field in this theory is consistent with dynamo waves that, according to the sign rule of Parker (1955) and Yoshimura (1975), propagate in the direction of

$$\boldsymbol{s}=\alpha\nabla\Omega\times\hat{\boldsymbol{e}}_{\phi}, \tag{1}$$

where $\hat{\boldsymbol{e}}_{\phi}$ is the unit vector in the azimuthal direction. The validity of this rule has been extensively tested in two-dimensional kinematic mean-field models (see, e.g., Charbonneau 2010). For the solar rotation inferred from helioseismology (Schou et al. 1998), the signs of the $\nabla\Omega$ components are well known. The sign of α estimated for granular convection is positive (negative) in the northern (southern) hemisphere. These properties favor a dynamo process distributed over the entire convection zone with the photospheric evolution shaped by the near-surface shear layer (NSSL) (Brandenburg 2005; Pipin & Kosovichev 2011). Alternative, flux-transport dynamo models in which the surface evolution is shaped by the

dynamics at the tachocline (and magnetic buoyancy) require coherent meridional motions directed equatorward at or slightly below the tachocline.

Different observational techniques have revealed a well-organized, though fluctuating, poleward meridional flow at the solar surface (e.g., Ulrich 2010; Hathaway 2012) with amplitudes of about $15\,\mathrm{m\,s^{-1}}$. However, recent inferences from helioseismology have determined the existence of two or more cells in the radial direction (Schad et al. 2013; Zhao et al. 2013). Thus, the existence of a coherent equatorial flow, able to transport the magnetic flux from the poles to the latitudes of sunspot activity, is unlikely.

The sign rule for propagation of dynamo waves remains valid also for mean-field models considering the dynamical evolution of the α-effect (Guerrero et al. 2010). In these models the kinetic component of the α-effect changes in time due to the backreaction of the magnetic field on the plasma motion. The magnetic α-effect depends on the distribution of the small-scale current helicity, and is a consequence of the conservation of magnetic helicity (Pouquet et al. 1976). It is regularly assumed that it diminishes the inductive action of the kinetic helicity (e.g., Sur et al. 2007; Guerrero et al. 2010; Mitra et al. 2011). For high magnetic Reynold numbers, this contribution can lead to the total suppression of the dynamo action, so-called catastrophic quenching, in the case when there is no effective mechanism to remove the small-scale current helicity (Guerrero et al. 2010). Recent works (Vishniac & Shapovalov 2014), and the results that will be presented here, indicate that this is not necessarily the only case, and that the magnetic contribution to the α-effect could be a source of magnetic field. A similar idea is suggested by Bonanno (2013).

Several kinematic or dynamic mean-field models have qualitatively reproduced the observed surface features of the solar magnetic field (Dikpati & Gilman 2001; Chatterjee et al. 2004; Guerrero & De Gouveia Dal Pino 2008; Pipin & Kosovichev 2011, 2013). Based on these models, Jouve et al. (2010) and Pipin (2015) have also studied dynamos for solar-like stars with the aim of reproducing observed trends for magnetic field strengths and cycle periods. Unfortunately, parameters like helicity and/or turbulent diffusion, in general, are poorly determined, and thus the physics of solar and stellar dynamos cannot be described unambiguously by the mean-field models. An alternative approach is provided by global 3D magnetohydrodynamic (MHD) simulations. In this class of modeling, even though the parametric regime is still far from the conditions of stellar interiors, the physics is self-consistently described and provides an important insight into the turbulent dynamics and dynamo.

For instance, systematic hydrodynamic (HD) studies of rotating turbulent convection, for the Sun and solar-like stars, have found that the Rossby number, $Ro = u_{\rm rms}/2\Omega_0 L$ (where Ω_0 is the frame rotation rate, L the characteristic large-scale length of the flow, and $u_{\rm rms}$ the typical turbulent velocity), characterizes the resulting mean flows (Gilman 1976; Glatzmaier & Gilman 1982; Steffen & Freytag 2007; Käpylä et al. 2011; Matt et al. 2011; Guerrero et al. 2013; Gastine et al. 2014; Featherstone & Miesch 2015). For large values of Ro the models result in an antisolar differential rotation (with faster rotating poles and a more slowly rotating equatorial region), and a meridional circulation with single cells per hemisphere. In the models with small values of Ro the differential rotation is solar-like, and the meridional flow consists of several circulation cells per hemisphere. The transition between these regimes is sharp, occurring in a narrow range of Ro. Several properties of the observed solar differential rotation, like the latitudinal dependence of the angular velocity, the tachocline (Ghizaru et al. 2010), and a NSSL, although so far only at high latitudes (Guerrero et al. 2013; Hotta et al. 2015), have been successfully reproduced.

MHD global dynamo models, which have been developed for more than a decade (e.g., Brun et al. 2004), have provided a wide spectrum of results, but the understanding of the dependence of the mean flows or magnetic fields on stellar parameters is still incomplete. Furthermore, to our knowledge, no MHD model so far has been able to reproduce the solar differential rotation.

MHD simulations of fast rotating stars by Brown et al. (2010) have been able to obtain large-scale dynamo action. Their results revealed a steady magnetic field organized in the shape of a torus, or wreaths, around the equator and with opposite polarity accros the hemispheres. Non-oscillatory dynamo solutions have also been obtained by Simitev et al. (2015). Oscillatory dynamo solutions in the global MHD models were first obtained by Ghizaru et al. (2010) using the EULAG-MHD code with an implicit sub-grid scale (SGS) formulation. Since then other groups have been able to simulate magnetic cycles with the use of SGS turbulent models (Augustson et al. 2013), or also in higher-resolution simulations by considering only a fraction (a wedge) of the star (Käpylä et al. 2012; Warnecke et al. 2014). Although the dynamo regimes of these models are not the same, it is noteworthy that the cycle periods obtained in the model of Ghizaru et al. (2010) and the models of Käpylä et al. (2012), Augustson et al. (2013), and Warnecke et al. (2014) are rather different. As will be shown later in this paper, this difference may be explained by the absence of a tachocline and a radiative stable layer in the models of Käpylä et al. (2012), Augustson et al. (2013), and Warnecke et al. (2014). By considering a forcing function to impose a constant angular velocity at the bottom of the domain, Browning et al. (2006) analyzed the effects of a tachocline in convective dynamo simulations. Although they found development of a strong toroidal magnetic field at this imposed shear layer, they observed no field reversals. Masada et al. (2013) explored the effects of penetrative convection in spherical dynamo simulations. Due to dissipative effects the tachocline obtained in their model is not well-defined. However, they obtained a stronger and cyclic large-scale toroidal magnetic field, demonstrating the importance of the stable layer in the storage of the magnetic field.

In this paper we compare 3D global MHD convective dynamo simulations with different Ro for models with and without the tachocline. Our goal is to compare the global properties of the mean flows and the resultant magnetic activity, and contrast them with observational signatures. Of particular interest are the inductive and diffusive terms resulting from the differential rotation and the collective effects of turbulence. Altogether, this will allow us to elucidate the importance of the tachocline in solar and stellar dynamos.

2. THE MODEL

We adopt a full spherical shell, $0 \leqslant \phi \leqslant 2\pi$, $0 \leqslant \theta \leqslant \pi$; the radial domain has its bottom boundary at $r_{\rm b} = 0.61\,R_\odot$ for the models that develop a tachocline, and $r_{\rm b} = 0.72\,R_\odot$ for the

models without it, and the upper boundary at $r_t = 0.96\,R_\odot$. Unlike Guerrero et al. (2013), where the anelastic equations of Lipps & Hemler (1982) were employed, here we solve their MHD extension (Ghizaru et al. 2010):

$$\boldsymbol{\nabla}\cdot(\rho_s\boldsymbol{u}) = 0, \tag{2}$$

$$\frac{D\boldsymbol{u}}{Dt} + 2\boldsymbol{\Omega}\times\boldsymbol{u} = -\boldsymbol{\nabla}\left(\frac{p'}{\rho_s}\right) + \boldsymbol{g}\frac{\Theta'}{\Theta_s} + \frac{1}{\mu_0\rho_s}(\boldsymbol{B}\cdot\nabla)\boldsymbol{B}, \tag{3}$$

$$\frac{D\Theta'}{Dt} = -\boldsymbol{u}\cdot\boldsymbol{\nabla}\Theta_e - \frac{\Theta'}{\tau}, \tag{4}$$

$$\frac{D\boldsymbol{B}}{Dt} = (\boldsymbol{B}\cdot\nabla)\boldsymbol{u} - \boldsymbol{B}(\nabla\cdot\boldsymbol{u}), \tag{5}$$

where $D/Dt = \partial/\partial t + \boldsymbol{u}\cdot\boldsymbol{\nabla}$ is the total time derivative, $\boldsymbol{u}$ is the velocity field in a rotating frame with $\boldsymbol{\Omega} = \Omega_0(\cos\theta, -\sin\theta, 0)$, p' is a pressure perturbation variable that accounts for both the gas and magnetic pressure, $\boldsymbol{B}$ is the magnetic field, and Θ' is the potential temperature perturbation with respect to an ambient state Θ_e (see Section 3 of Guerrero et al. 2013, for a comprehensive discussion). Furthermore, ρ_s and Θ_s are the density and potential temperature of the reference state, which is chosen to be isentropic (i.e., $\Theta_s = \text{const}$) and in hydrostatic equilibrium; $\boldsymbol{g} = GM/r^2\hat{\boldsymbol{e}}_r$ is the gravity acceleration, G and M are the gravitational constant and the stellar mass, respectively, and μ_0 is the magnetic permeability. The potential temperature, Θ, is related to the specific entropy: $s = c_p \ln\Theta + \text{const}$.

The term Θ'/τ represents the balancing action of the turbulent Reynolds heat flux responsible for maintaining the steady axisymmetric solution of the stellar structure (see Section 1.2 and Annexe B in Cossette 2015, for details). In this work the parameters of the ambient state are slightly different from those in Equation (7) of Guerrero et al. (2013, Section 3.1). For the models including a tachocline, here we use the polytropic indices $m_r = 2$ and $m_{cz} = 1.499978$, together with the transition width $w_t = 0.015\,R_\odot$. In the models without a tachocline, the polytropic index is constant, $m_{cz} = 1.499985$. These values result in convective motions with similar *Ro* for both types of models. The relaxation time of the potential temperature perturbation for all models is $\tau = 1.036 \times 10^8$ s (~3.3 yr).

The equations are solved numerically using the EULAG-MHD code (Ghizaru et al. 2010; Racine et al. 2011; Guerrero et al. 2013; Smolarkiewicz & Charbonneau 2013), a spin-off of the hydrodynamic model EULAG predominantly used in atmospheric and climate research (Prusa et al. 2008). The time evolution is calculated using a special semi-implicit method based on a high-resolution, non-oscillatory forward-in-time advection scheme known as Multidimensional Positive Definite Advection Transport Algorithm (MPDATA; Smolarkiewicz 2006). The truncation terms in MPDATA evince viscosity comparable to the explicit SGS viscosity used in large-eddy simulation (LES) models (Elliott & Smolarkiewicz 2002; Domaradzki et al. 2003; Margolin et al. 2006). Thus, the results of MPDATA are often interpreted as implicit LES or ILES (Smolarkiewicz & Margolin 2007).

For the velocity field we use impermeable, stress-free conditions at the top and bottom surfaces of the shell, whereas the magnetic field is assumed to be radial at these boundaries. Finally, for the thermal boundary condition we consider zero divergence of the convective flux at the bottom and zero flux at the top surface.

3. RESULTS

We have performed two sets of simulations: (1) only for the unstable stratified convection zone (CZ models), and (2) for the convection zone with a convectively stable radiative zone at the bottom of the domain (RC models). The first set does not support the formation of a strong radial shear at the base of the convection zone (the tachocline), and thus excludes it as a source of magnetic field. The second set naturally leads to the development of a tachocline and therefore to the $(\boldsymbol{B}\cdot\nabla)\Omega$ source of the toroidal field acting in the tachocline. The input and resulting parameters of the models for three different rotation rates, Ω_0 (corresponding to different *Ro*)[6] are summarized in Table 1.

3.1. Dynamo Models without Tachocline

In Figure 1 we present, from left to right, the meridional profiles of the differential rotation, meridional circulation, and snapshots of the vertical velocity, u_r, and the toroidal magnetic field B_ϕ resulting from the models (a) CZ01, (b) CZ02, and (c) CZ03. The differential rotation and meridional circulation correspond to averages over longitude and time (~3 yr). The instantaneous orthographic projections of u_r and B_ϕ allow us to distinguish the character of the convective flow and the distribution of the toroidal field for each model. Unlike our previous purely hydrodynamic simulations, in which we found a critical *Ro* value dividing the rotation profiles into solar-like and antisolar rotation types (Guerrero et al. 2013), in the present simulations with magnetic field all the models exhibit the solar-like differential rotation, irrespective of *Ro*. This property is related to the influence of the dynamo-generated magnetic field on the fluid dynamics. Karak et al. (2015) have found that for the MHD case the transition occurs at higher values of *Ro*. For instance, model CZ01 shows iso-rotation contours mainly aligned along the rotation axis (see Figure 1(a)). In models CZ02 (Figure 1(b)) and CZ03 (Figure 1(c)) the rotation profile exhibits clear conical-shape contours that resemble the rotation of the solar convection zone inferred by helioseismology (Schou et al. 1998). During early stages of the models' evolution, when the influence of the magnetic field is negligible, the rotation contours are aligned along the rotation axis (the so-called Taylor–Proudman balance), and then transformed into the conical-shape contours. This indicates that both Reynolds and Maxwell stresses contribute to the distribution of angular momentum. Later, it is remarkable that even in model CZ03, in which the final magnetic energy is 10^4 times smaller than the kinetic energy, the rotation law departs from the Taylor–Proudman balance. A detailed discussion of the angular momentum balance is out of the scope of this paper and will be addressed in a subsequent paper.

Another remarkable feature of models CZ02 and CZ03 is the natural development of a well-defined NSSL. The radial shear in this layer is negative and extends from the equator to the poles as observed in the Sun. In agreement with the results found in Guerrero et al. (2013), the NSSL arises from the

[6] Since we change the value of *Ro* only by changing the value of the frame rotation rate, we use both terms interchangeably to express the dependence of the results on Ω_0.

Table 1
Simulation Parameters and Outputs

Model	Ω_0	Ro	Ra^*	u_{rms}	Ma (10^{-4})	χ_Ω	λ	e_M/e_K	e_ϕ/e_K	e_p/e_K	T_M
CZ01	$2\Omega_\odot$	0.030	1.29	55.12	3.85	0.09	2.26	0.098	0.080	0.018	2.26
CZ02	$\Omega_\odot$	0.067	5.16	60.91	4.25	0.17	0.65	0.010	0.009	0.001	2.21
CZ03	$\Omega_\odot/2$	0.150	20.65	67.18	4.69	0.18	0.56	$2{\cdot}10^{-4}$	$2{\cdot}10^{-4}$	$1{\cdot}10^{-5}$	⋯
RC01	$2\Omega_\odot$	0.033	1.36	60.80	4.10	0.07	0.84	0.249	0.042	0.206	⋯
RC02	$\Omega_\odot$	0.069	5.45	62.27	4.30	0.05	0.85	0.184	0.163	0.020	34.5
RC03	$\Omega_\odot/2$	0.161	21.80	72.88	5.04	0.28	0.06	0.004	0.004	$3{\cdot}10^{-4}$	⋯

Note. $Ra^* = \frac{1}{c_P \Omega_0^2} g \frac{\partial s_e}{\partial r}$, where s_e is the specific entropy of the ambient state, u_{rms} is the volume-averaged rms velocity (in m s^{-1}) in the unstable layer, $Ma = u_{rms}/c_s^*$ is the Mach number, with $c_s^* = \sqrt{\gamma R T_s^*}\,|_{r=0.85R_\odot}$ being the sound speed at the middle of the unstable layer, $Ro = \frac{u_{rms}}{2\Omega_0 L}$, and $\chi_\Omega = (\Omega_{eq} - \Omega_p)/\Omega_0$, where $\Omega_{eq} = \overline{\Omega}(R_\odot, 0°)$ and $\Omega_p = \overline{\Omega}(R_\odot, 60°)$ are the surface rotation rates at 0° and 60° in latitude, and Ω_0 is the frame rotation rate expressed in terms of the solar rotation rate $\Omega_\odot$. The growth rate of the magnetic field, λ, is given in Tesla yr^{-1}. The kinetic and magnetic energy densities, in J m^{-3}, are $e_K = \overline{\rho}_s \overline{\boldsymbol{u}}^2/2$, $e_M = \overline{\boldsymbol{B}}^2/2\mu_0$, $e_\phi = \overline{B}_\phi^2/2\mu_0$, and $e_p = (\overline{B}_r^2 + \overline{B}_\theta^2)/2\mu_0$. Finally, the full cycle period, T_M, is expressed in years. Models starting with the letters CZ consider the convection zone only, while models starting with RC include both radiative and convective zones. The number of grid mesh points is $N_r = 47$, $N_\theta = 64$, and $N_\phi = 128$ for CZ models, and $N_r = 64$ for RC models.

appropriate choice of the ambient state, Θ_e, and the relaxation time of the potential temperature perturbations, τ. As mentioned above, these quantities differ from the ones used in Guerrero et al. (2013) in such a way that *Ro* becomes larger at the top of the domain (i.e., in a thin layer close to the surface where the buoyancy force becomes much stronger than the Coriolis force). Although the number of mesh points is not sufficient to resolve supergranulation scales that may be important for the formation of the solar NSSL, our model succeeded in reproducing similar effects in the resolved scales. Furthermore, the latitudinal angular velocity gradient in both models corresponds well to the solar rotation, i.e., $\chi_\Omega = (\Omega_{eq} - \Omega_p)/\Omega_0 = 0.18$, where Ω_{eq} is the equatorial angular velocity, Ω_p is the angular velocity at 60° latitude (both quantities are computed from the temporally and azimuthally averaged profile of Ω), and Ω_0 is the angular velocity of the reference frame.

As far as the meridional circulation is concerned, models CZ01 and CZ02 show a multicellular pattern (second column of Figures 1(a) and (b)), while model CZ03 shows a dominant (counter)clockwise cell in the (northern) southern hemisphere with a latitudinal velocity, $u_\theta \sim 12$ m s^{-1} (about twice the value of u_θ in models CZ01 and CZ02). This cell is located near the base of the convection zone. Another cell, with a smaller velocity and opposite direction of circulation appears in the subsurface layer (second column of Figure 1(c)).

An oscillatory large-scale dynamo action is observed in models CZ01 and CZ02 as can be seen in Figures 2(a) and (b). In both cases the toroidal magnetic field is generally symmetric across the equator and reverses with a cycle period of ∼2 yr (Table 1). For the model CZ02 we found a secondary ∼6 yr cycle modulating the amplitude of the magnetic field. These properties are at odds with the 22 yr solar cycle but in agreement with other global models without a tachocline (e.g., Warnecke et al. 2014; Augustson et al. 2015). In the convection zone the evolution of the magnetic fields is consistent with a pattern of dynamo waves propagating from the bottom to the top of the domain (Figures 2(a), (b)). At the surface the field forms a ±50° belt around the equator. The latitudinal migration of the field is slightly poleward. The long-term evolution of the simulations CZ01 and CZ02 indicates extended periods of minimal or maximal activity (see for instance the extended minimum in the northern hemisphere of the model CZ01 in Figure 2(a) between 20 and 30 yr). The amplitude of the dynamo-generated magnetic field depends on the rotation rate, reaching ∼10% and ∼1% of the kinetic energy of the system, for the models CZ01 and CZ02, respectively (see Table 1). In model CZ03 (Figure 2(c)) the magnetic field grows exponentially but saturates at ∼0.02% of the kinetic energy (see Table 1). The magnetic field in this case is nearly steady. Its time evolution shows periods when the field amplitude abruptly decays, stays in a minimum state for some years, and then quickly grows again to its saturation amplitude without polarity reversals (Figure 2(c)). As indicated in Table 1, the growth rate of the dynamo is proportional to the rotation rate.

The spatio-temporal evolution of the magnetic field in the models can be interpreted in terms of its main sources according to the mean-field dynamo theory, i.e., the α and Ω effects. The profile of α is estimated by using the first-order smoothing approximation (FOSA, see Brandenburg & Subramanian 2005 for details) as follows:

$$\alpha = \alpha_k + \alpha_m = -\frac{\tau_c}{3} h_k + \frac{\tau_c}{3} h_c, \tag{6}$$

where $\tau_c = H_\rho/u_{rms}$ is the turnover time of the convection, $H_\rho^{-1} = d\ln\rho_s/dr$ is the density length scale, and

$$h_k = \overline{\boldsymbol{u}' \cdot \nabla \times \boldsymbol{u}'}$$
$$h_c = \frac{\overline{\boldsymbol{b}' \cdot \nabla \times \boldsymbol{b}'}}{\mu_0 \rho_s} \tag{7}$$

are the small-scale (note the prime over $\boldsymbol{u}$ and $\boldsymbol{b}$) kinetic and current helicities, respectively (the overbars denote azimuthal and temporal averages over three years). As is common in the mean-field dynamo theory, we present the source terms as ratios between the induction and diffusion times:

$$C_\alpha^k = \frac{\alpha_k R_\odot}{\eta_{t0}}, \quad C_\alpha^m = \frac{\alpha_m R_\odot}{\eta_{t0}},$$
$$C_\Omega^r = \frac{\partial_r \Omega R_\odot^3}{\eta_{t0}}, \quad C_\Omega^\theta = \frac{\partial_\theta \Omega R_\odot^3}{r\eta_{t0}}, \tag{8}$$

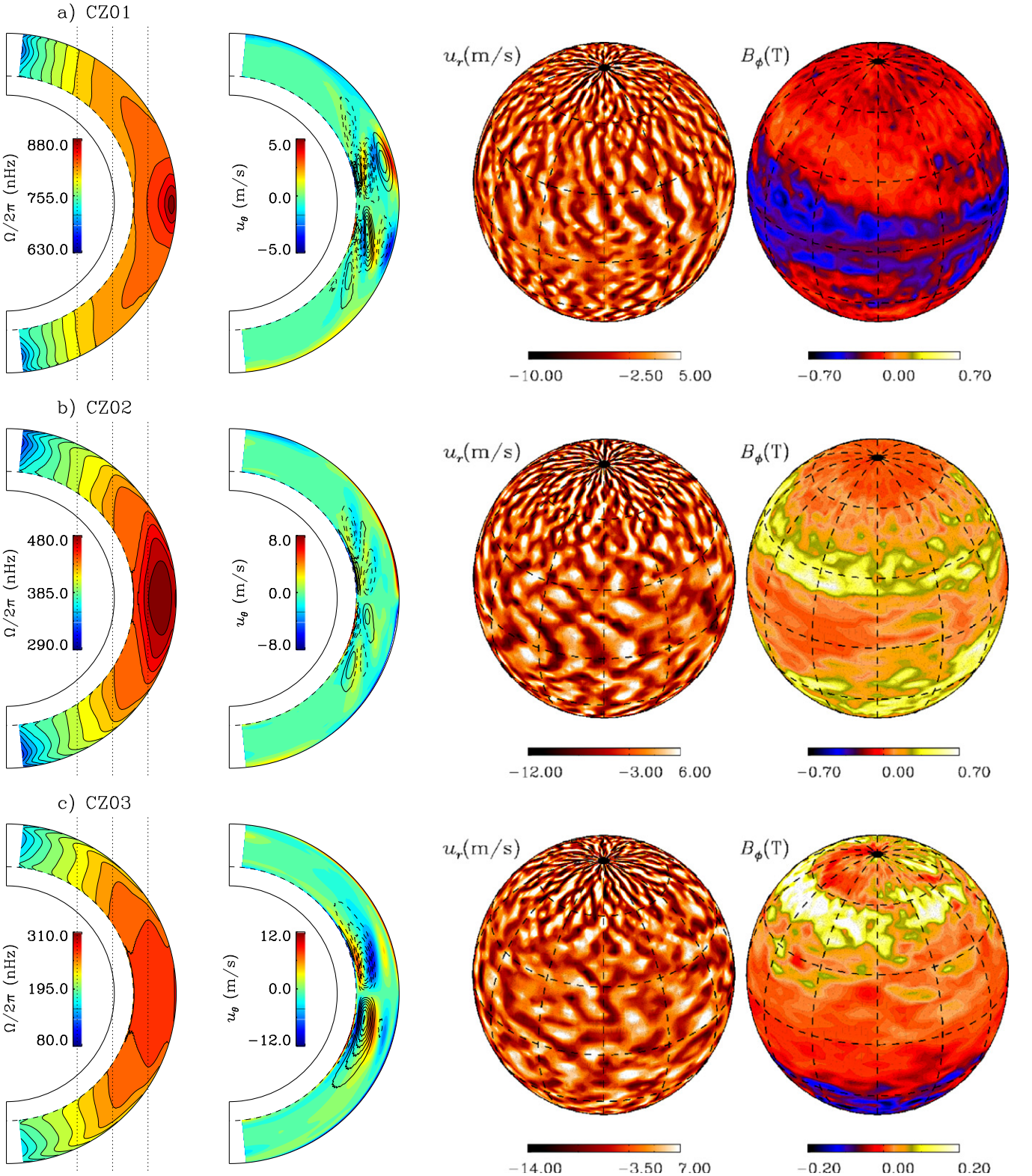

Figure 1. From left to right: mean profiles of the rotation rate and meridional circulation, and snapshots at $r = 0.95R_\odot$ of the vertical velocity, u_r, and the toroidal field, B_ϕ, for the simulated models (a) CZ01, (b) CZ02, and (c) CZ03. In the meridional circulation panels continuous (dashed) lines correspond to clockwise (counterclockwise) circulation. The background filled contours show the latitudinal velocity, $\overline{u}_\theta$. The profiles of differential rotation and meridional circulation correspond to mean azimuthal values averaged over ∼3 yr during the steady-state phase of the simulation.

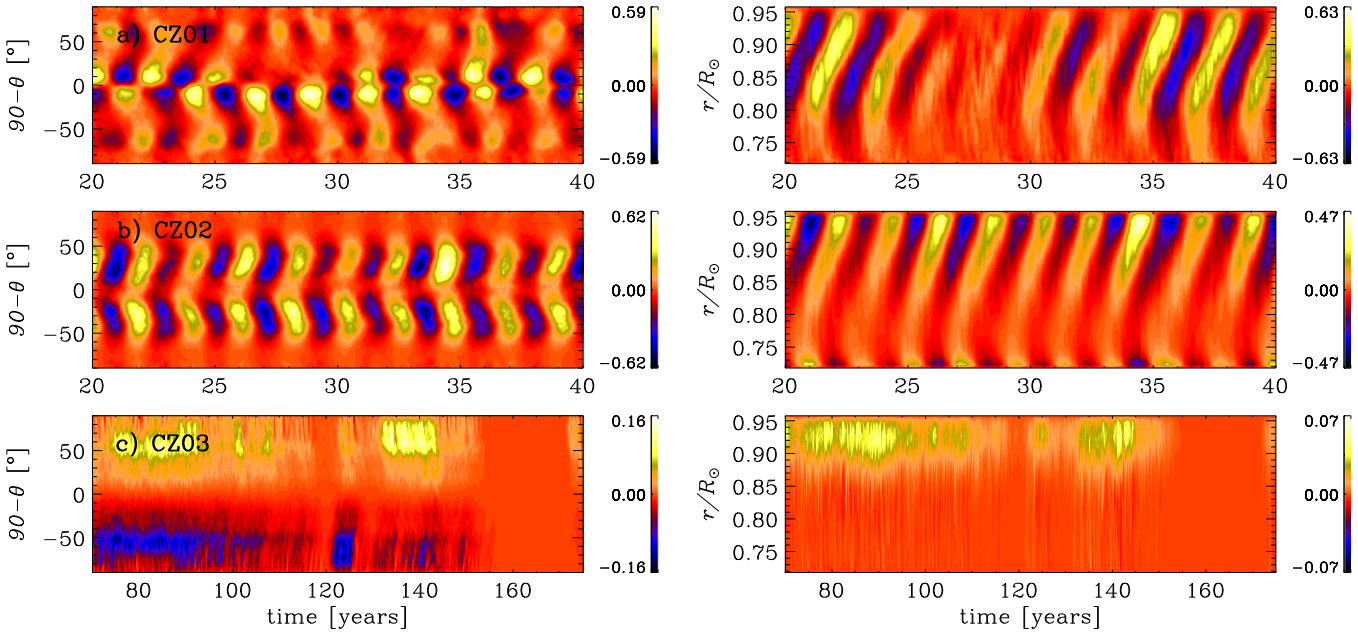

Figure 2. Time–latitude (left) and time–radius (right) diagrams of the toroidal magnetic field, $\overline{B}_\phi$, for models (a) CZ01, (b) CZ02, and (c) CZ03. On the left, the contours show $\overline{B}_\phi$, in tesla, at $r = 0.95R_\odot$. On the right, the contours are taken at 30° latitude. Only a fraction of time of the simulated statistically steady state is shown in each plot.

where η_{t0} is the FOSA estimation of the turbulent magnetic diffusivity,

$$\eta_{t0} = \frac{1}{3}\tau_c u_{\rm rms}^2, \tag{9}$$

averaged over the entire convection zone, $0.72\,R_\odot \leqslant r \leqslant 0.96R_\odot$ (the values of η_{t0} are presented in Table 2).

In the top, middle, and bottom rows of Figure 3 we present the normalized profiles of α, $\partial_r\Omega$, and $r^{-1}\partial_\theta\Omega$, respectively, computed from the simulation results. Figure 3(a) shows the radial profiles of the kinetic and magnetic contributions to α presented by dotted and dotted–dashed lines, respectively, while the resultant α is shown with continuous lines. The vertical profiles of the radial shear, Figure 3(c), are shown at two different ranges of latitude: a higher latitude profile (dashed lines) was computed by averaging over 60° and 80° latitude, and the lower latitude profile (continuous line) was averaged between 20° and 40° latitude. Finally, the latitudinal shear was also computed for two different ranges of depths, Figure 3(e). The bottom profile (dashed line) corresponds to an average over $0.72\,R_\odot \leqslant r \leqslant 0.77\,R_\odot$, while the top profile (continuous line) is an average over $0.90\,R_\odot \leqslant r \leqslant 0.95\,R_\odot$. Presenting these quantities as radial profiles, instead of contours in the meridional plane, allows us to straightforwardly compare the different dynamo models. The red, blue, and green lines correspond to models 01, 02, and 03, respectively. Furthermore, Figure 3 allows us to directly compare the CZ and RC models (to be discussed later), shown in the left and right panels, respectively.

Before describing the evolution of the magnetic fields, it is instructive to discuss how the source terms change as a function of *Ro*. Table 2 presents the maximal absolute values of the quantities depicted in Figure 3 (denoted with a subsscript zero), as well as the maximal amplitude of the mean magnetic field components at the surface level. (Some values at the boundaries can be very large without really contributing to the dynamo, so we have disregarded them.) In general, there are no major differences between the profiles of the kinetic α-term, C_α^k. In all cases it is positive in the bulk of the convection zone and changes sign near the boundaries. The radius at which this change of sign occurs is shallower (deeper) for the faster (slower) rotating model. There is no clear relation between $C_{\alpha 0}^k$ and *Ro*; it is only noticeable, however, that the faster models, CZ01 and CZ02, have larger kinetic helicity than the slower model, CZ03. As for the the magnetic α-effect, we should first notice that its amplitude is comparable to the kinetic α. However, $C_{\alpha 0}^m$ is inversely proportional to *Ro*. This is expected since the models with faster rotation develop stronger magnetic fields. Correspondingly, the total α-effect is inversely proportional to *Ro*. For the models CZ01 and CZ02 the signs of C_α^k and C_α^m in the middle of the convection zone are opposite. At the top of the domain the two terms have the same sign, and both contribute positively to the generation of magnetic field. In model CZ03 the contribution of C_α^m is negligible, thus only the kinetic helicity contributes to the field generation.

Regarding the rotational shear terms, we notice that for larger values of *Ro*, the surface radial shear is stronger and the latitudinal shear is weaker. Note that the latitudinal profile of C_Ω^θ (Figure 3(e)) for model CZ01 shows a strong shear at the equator and the poles. This shear is reduced in models CZ02 and CZ03 as the vertical motions become more important. These fast vertical flows, in turn, are less affected by the Coriolis force, resulting in a strong radial shear in the NSSL. The surface values of the magnetic field are also inversely proportional to *Ro*, possibly indicating that their main source is the latitudinal shear.

The evolution of models CZ01 and CZ02, presented in the butterfly diagrams of Figures 2(a) and (b), is similar. They exhibit branches of magnetic field migrating in latitude from

Table 2
Dynamo Coefficients Computed from the Simulation Results

Model	$\eta_{t0}(10^9)$	$C_{\alpha 0}^{k}$	$C_{\alpha 0}^{m}$	$C_{\alpha 0}$	$C_{\Omega 0}^{r}(10^3)$	$C_{\Omega 0}^{\theta}$	D_r	D_θ	$\max(\overline{B}_\phi)$	$\max(\overline{B}_\theta)$	$\max(\overline{B}_r)$
CZ01	0.99	5.01	1.84	4.47	0.37	27.28	1.65	122.90	0.60	0.18	0.03
CZ02	1.09	5.38	1.28	5.00	1.62	14.75	8.10	73.75	0.61	0.13	0.06
CZ03	1.28	2.72	0.08	2,72	1.69	9.71	4.59	26.41	0.15	0.05	0.02
RC01	1.08	3.03	2.06	2.75	0.81	19.65	2.22	54.03	0.52(0.19)	0.10(0.80)	0.04(0.26)
RC02	1.12	2.80	1.52	2.72	1.67	13.33	4.54	36.25	0.22(0.94)	0.07(0.28)	0.03(0.24)
RC03	1.25	3.56	0.64	3.52	4.98	21.51	17.53	75.71	0.20(0.71)	0.04(0.37)	0.03(0.20)

Note. The dynamo numbers are computed with Equations (8) and (9). The subscript zero on C_α and C_Ω refers to the maximum value of each quantity, while on η_t it refers to its average over the CZ (in $m^2\ s^{-1}$). The dynamo numbers $D_r = C_{\alpha 0} C_{\Omega 0}^{r}$ and $D_\theta = C_{\alpha 0} C_{\Omega 0}^{\theta}$ provide an indication of the dynamo efficiency when considering the radial and the latitudinal shear, respectively. Finally, $\max(\overline{B}_\phi)$, $\max(\overline{B}_\theta)$, and $\max(\overline{B}_r)$ are the maximum absolute values of the large-scale components of the field at $r = 0.95\ R_\odot$ (the values in brackets are measured at $r = 0.72\ R_\odot$) in units of tesla.

the equator toward the poles. This pattern agrees with the Parker–Yoshimura sign rule, Equation (1), for positive values of $\alpha \partial_r \Omega$ in almost the entire convection zone (see continuous red and blue lines in Figures 3(a), (c)). In the vertical direction the propagation of the magnetic field in the middle of the CZ also agrees with Equation (1) for $\alpha \partial_\theta \Omega > 0$. Because of the large values of C_Ω^θ in model CZ01, the branches of toroidal field show a large magnetic field strength from the bottom of the convection zone to the top. In model CZ02, with a smooth latitudinal shear the stronger vertical branches of $\overline{B}_\phi$ start at a depth $\sim 0.85 R_\odot$ (compare the right panels of Figures 2(a) and (b)). At the upper radial levels of model CZ02, the term $\alpha \partial_\theta \Omega$ becomes negative, and this should change the direction of migration. However, at the latitude depicted in Figure 2, only a slight change in the tilt of the branches is evident. The morphology of the azimuthally averaged magnetic field of model CZ02 is depicted in Figures 4(a)–(d). The filled contours show the positive (yellow) and negative (blue) toroidal field strength. The continuous (dashed) lines represent the clockwise (counterclockwise) poloidal field lines. The four snapshots cover one magnetic field reversal. In the same plot it can be observed that the poloidal field follows a wave-like evolution pattern similar to $\overline{B}_\phi$. The pattern starts to develop at the bottom of the domain at lower latitudes. As the cycle evolves it grows and expands over the convection zone with the more intense regions (the innermost contours) migrating poleward and upward. In this case, however, the field is antisymmetric with respect to the equator.

3.2. Dynamo Models with a Tachocline

In this section we present three models (RC01, RC02, and RC03) with the tachocline. All of them have the same stratification and differ only by the rotation rate, Ω_0. For all these cases, the magnetic field evolves differently than in the models CZ01, CZ02, and CZ03.

It is worth mentioning first that, due to the presence of the tachocline, most of the magnetic field develops at the base of the convection zone. Thus, the Maxwell stresses play an important role in the downward transport of the angular momentum. In Figure 5, panels (a), (b), and (c) show the differential rotation (left column) and meridional circulation (right column) profiles of models RC01, RC02, and RC03, respectively. Model RC01 has the lowest value of *Ro*, thus it has the strongest influence of the Coriolis force. This force tends to homogenize the rotation of the convection zone with that of the radiative zone. This happens in a region between $\sim 5^\circ$ and $\sim 80^\circ$ latitude. However, zones with some radial and latitudinal shears develop at the equatorial and polar latitudes. In model RC02, both radial and latitudinal differential rotations develop in larger zones. The intermediate latitudes are in iso-rotation with the radiative zone.

The transport of angular momentum to the radiative zone makes the stable layer rotate, on average (see Figure 5(b)), faster than the frame. Hence, the equatorial acceleration of the convection zone in the model RC02 is not as pronounced as in the model CZ02. In the former case the angular velocity is around 440 nHz, while in the latter case it reaches 500 nHz. Consequently, the latitude of iso-rotation with the frame moves up to $\sim 70^\circ$. In the model CZ02 it is located at $\sim 50^\circ$ (the yellow filled contours in Figures 1(b) and 5(b) correspond approximately to the frame rotation rate, Ω_0).

Besides affecting the average profile of the differential rotation (with respect to purely hydrodynamic models) the magnetic feedback on the flow generates torsional oscillations in the models where the dynamo is periodic (CZ02 and RC02). The latitudinal morphology of the simulated oscillations resembles the solar observations, but the amplitude of the observed oscillations is a few times smaller. This might be a consequence of a rather large α-effect such as found by Covas et al. (2004). The origin of the torsional oscillations in our simulations seems to be due to a modulation of the latitudinal angular momentum transport mediated by the meridional circulation and the magnetic torque (at equatorial latitudes). A comprehensive discussion of these results is beyond the scope of the current work and is presented in a separate paper (G. Guerrero et al. 2016, in preparation).

An NSSL, more pronounced at higher latitudes, is also observed in this model (RC01). In both RC01 and RC02 the contours of rotation form conical shapes in the convection zone (see the vertical dotted lines in Figure 5 as a guide to the eye). Finally, in model RC03 there is a well-defined latitudinal differential rotation in the bulk of the convection zone, and also a NSSL is formed. The region of iso-rotation of the convection zone with the radiative core occurs at higher latitudes ($\sim 70^\circ$). For this reason the radial shear at the equator, in the tachocline, is stronger in model RC03 than in models RC01 and RC02. The contours of model RC03 appear cylindrical, which is surprising because in this model the influence of the Coriolis force is smaller than in the other two cases. The rightmost columns of Figure 5 show the convective structure, represented by the vertical velocity and the distribution of the toroidal field at $r = 0.95 R_\odot$.

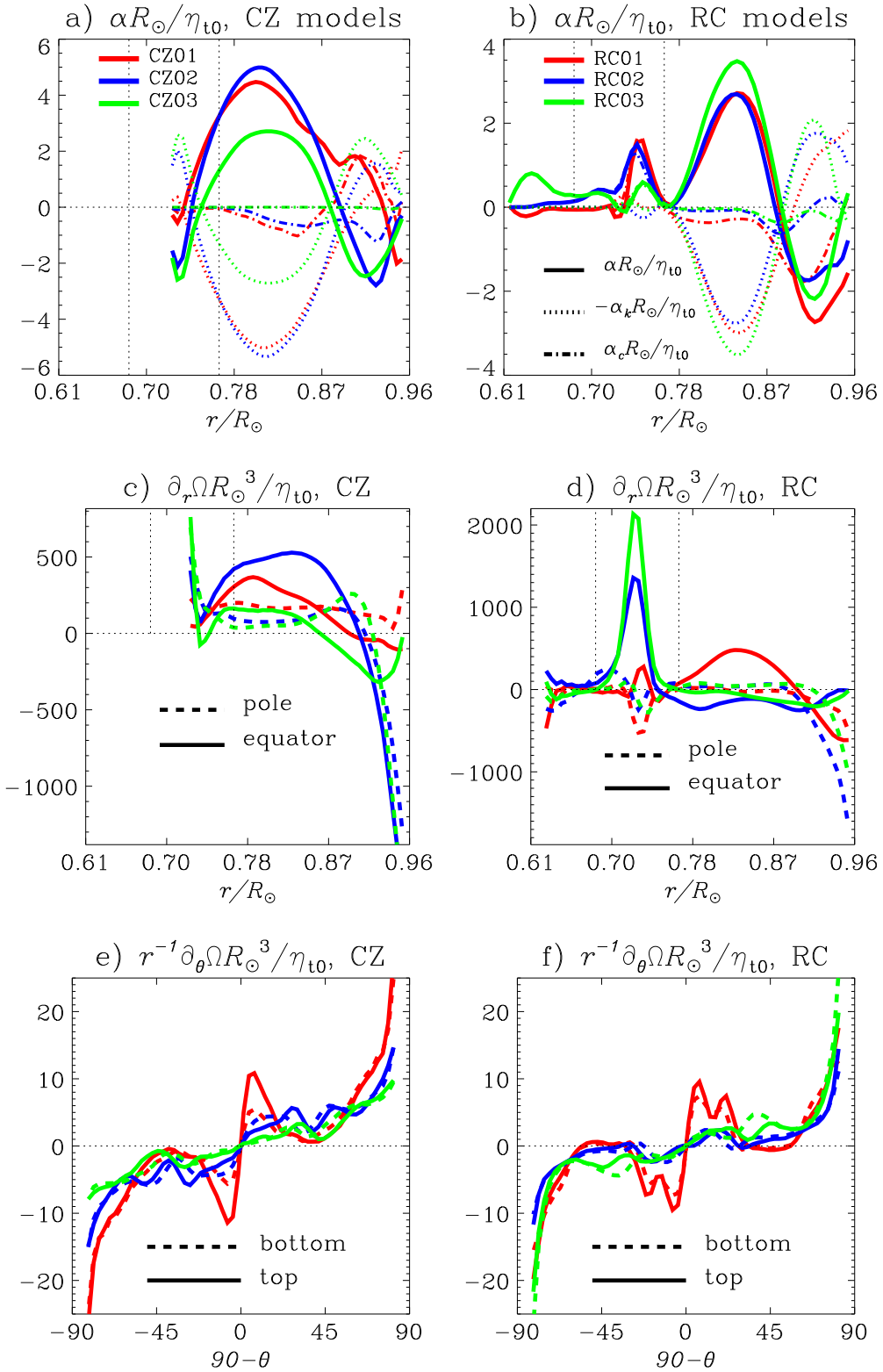

Figure 3. Magnetic field source terms (see Equations (8)–(9)) for models CZ (left panels) and RC (right). Panels (a) and (b) show the FOSA estimation for $\alpha\ R_\odot/\eta_{t0}$. Dotted and dotted–dashed lines represent the kinetic and magnetic contribution, respectively. The continuous line is the resultant, non-dimensional, total α-effect. The profiles of α are latitudinal averages in the northern hemisphere. Middle and bottom rows show $\partial_r \Omega\ R_\odot^3/\eta_{t0}$ and $r^{-1}\partial_\theta \Omega\ R_\odot^3/\eta_{t0}$, respectively. In panels (c) and (d) continuous (dashed) lines indicate latitudinal averages at lower, 20°–40° (higher, 60°–80°), latitudes. (Note that in panel (d) the value of $\partial_r \Omega\ R_\odot^3/\eta_{t0}$ for the model RC03 has been divided by 2.) In panels (e) and (f) continuous (dashed) lines are vertical averages in the top, $0.9\ R_\odot \leqslant r \leqslant 0.95\ R_\odot$ (bottom, $0.72\ R_\odot \leqslant r \leqslant 0.77\ R_\odot$), of the domain. η_{t0} is a radial average of η_t, defined in Equation (9), for $r \geqslant 0.72 R_\odot$.

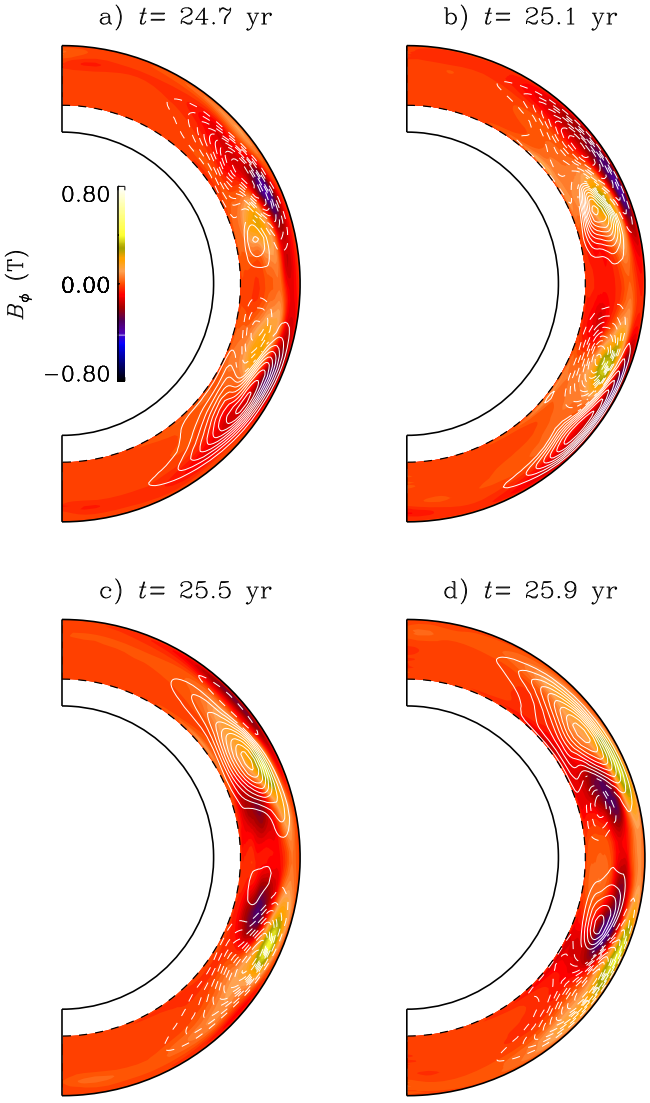

Figure 4. Snapshots of the mean magnetic fields, $\overline{B}_\phi$ (color images), and poloidal magnetic field (contour lines) for the model CZ02. Continuous (dashed) lines represent clockwise (counterclockwise) magnetic field direction. The time series covers one polarity reversal (half a dynamo cycle).

The meridional circulation is multicellular in all our models with the tachocline. However, as expected, model RC03 has larger meridional velocities than the other models and exhibits a dominant counterclockwise (clockwise) cell in the northern (southern) hemisphere. It is noteworthy that in all these models a low-amplitude poleward flow develops in the upper part of the convection zone at latitudes $>30°$. This can be noticed in the second column of Figure 5 in the color-filled contours of the latitudinal velocity, $\overline{u}_\theta$, as the blue and yellow regions in the northern and southern hemispheres, respectively. The formation of this flow is likely due to the gyroscopic pumping mechanism because of the negative gradient of angular velocity (Miesch & Hindman 2011).

The third column of Figure 5 shows that the smaller convective structures in our simulations are formed at higher latitudes. In the equatorial band the structures are elongated, resembling the so-called banana cells. Note that the vertical domain of our simulations reaches up to $0.96R_\odot$, and small-scale structures are not resolved. We surmise that this is the reason why NSSL and latitudinal meridional circulation only appear above $\sim 30°$ latitude. Nevertheless, the meridional flow structure qualitatively agrees with recent helioseismology inversions made using data from the *Solar Dynamics Observatory* (Schad et al. 2013; Zhao et al. 2013).

The magnetic field in these models evolves on longer timescales than in the CZ models (see Section 3.3). The fast rotating model, RC01, develops a magnetic field that oscillates in amplitude but does not show clear polarity reversals. The oscillation period is ~ 10 yr (not included in Table 1 because it does not correspond to magnetic field reversals). The topology of the field consists of wreaths of toroidal field of opposite polarity across the equator.

Model RC02 presents magnetic cycles with a full period of ~ 30 yr. Unlike the solar magnetic field, in this model the toroidal (poloidal) component of the magnetic field is symmetric (antisymmetric) relative to the equator (see Figures 6(b) and 7). Most of the magnetic energy in this case is in the toroidal component of the field. In the simulation with the slowest rotation rate (model RC03), the magnetic field is nearly steady (as in CZ03) with a larger concentration of $\overline{B}_\phi$ in a narrow region at the base of the convection zone at the equatorial latitudes. The field at the surface has the same polarity as at the bottom and is concentrated at higher latitudes.

An important disparity between the models RC and their non-tachocline counterparts, models CZ, is the ratio between their volume-averaged magnetic and kinetic energies, as can be seen in Table 1. This difference is absent in the surface layers where the two sets of models show magnetic fields of similar magnitude (in fact, models CZ have slightly higher values, see Table 2). In both CZ and RC cases, the amplitude of the surface field correlates directly with the rotation rate. Nevertheless, because of the radial shear at the tachocline, in the RC models the maximum mean field in that region reaches ~ 1 T (10^4 G), as evident in the right panels of Figure 6 and Table 2 (values in parenthesis).

As for the turbulent coefficients in these models, there is a clear correlation between the turbulent diffusion coefficient, η_{t0}, and the rotation rate, indicating that rotation quenches turbulent diffusion. However, while *Ro* changes by a factor of ~ 5 between the faster and slower models, η_{t0} changes by only a factor of ~ 1.15. Similar to the models CZ, there is no correlation between the kinetic α-effect and the rotation. Figure 3(b) shows that the radial profiles of C_α^k are roughly the same for the three models. They have small positive values at the radiative zone, reach a positive maximum in the middle of the convection zone, and change sign near the upper boundary. On the other hand, C_α^m changes proportionally to the rotation rate. The sign of C_α^m at the tachocline is positive, and it is the dominant term in the total α-effect in that region. In the lower/middle part of the convection zone the sign of C_α^m is opposite to C_α^k, but its amplitude is small. For models RC01 and RC02 in the upper convection zone C_α^m is negative and, because of the low density, reaches maximum values. Similarly to models CZ, both C_α^k and C_α^m contribute to the field generation. For the slowest rotating model, RC03, the contribution of C_α^m is unimportant.

Models RC develop strong radial shear at the interface between the radiative and convective layers (Figure 3(d)). This radial shear anticorrelates with the rotation rate, i.e., the slower the rotation rate, the largest the shear at the tachocline. Similar to the solar case, the radial shear at the tachocline is negative at

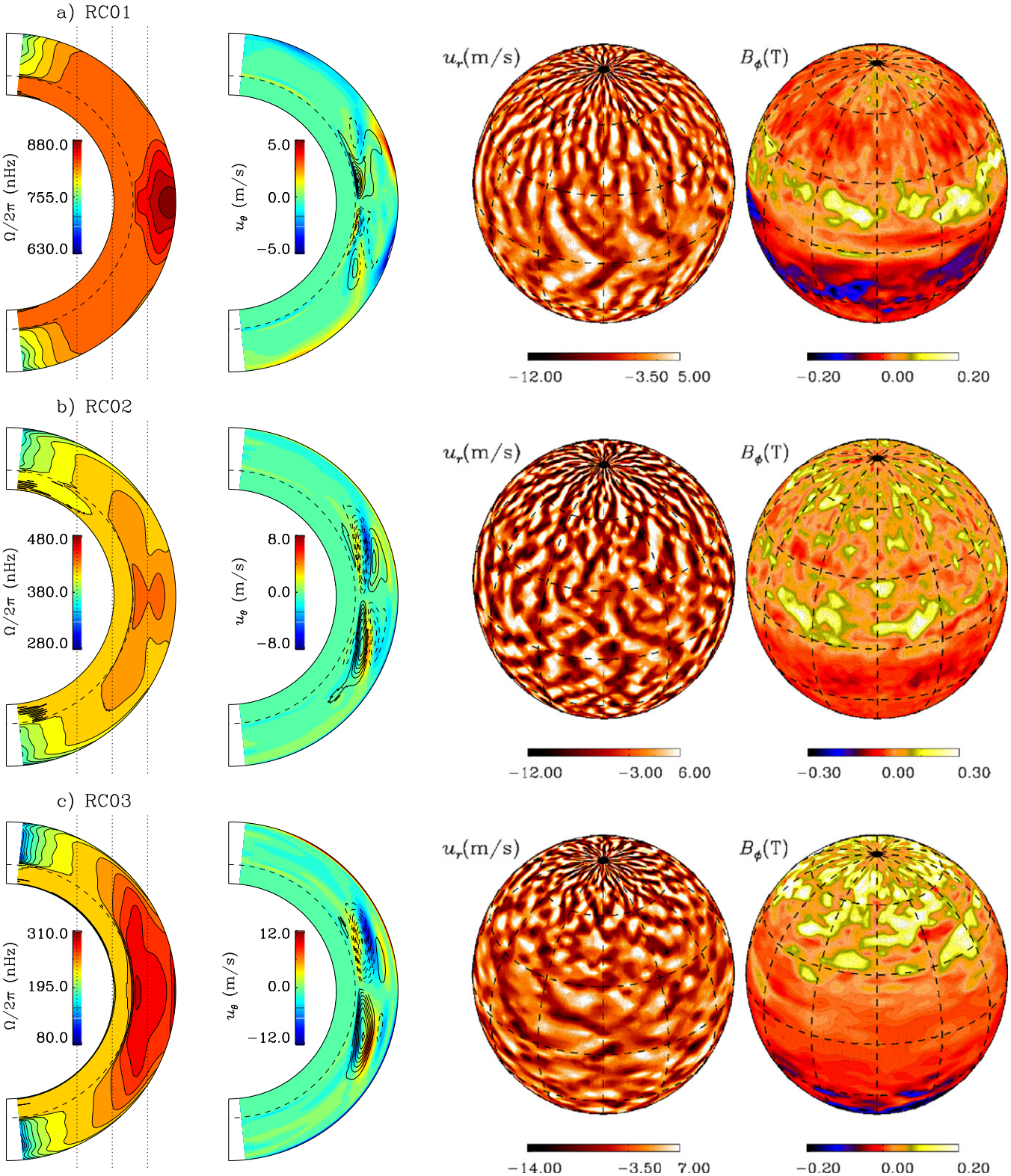

Figure 5. Same as Figure 1 but for the models (a) RC01, (b) RC02, and (c) RC03. For these cases the temporal average is over ∼10 yr during the steady-state phase of the simulation.

the poles and positive at the equator. According to helioseismology the Sun exhibits the strongest shear at the poles, whereas all the models in this section have the strongest shear at the equator. The profiles of $\partial_r\Omega$ are fairly flat in the convection zone and negative in the NSSL at high latitudes (Figure 3(d)). As for the latitudinal differential rotation, the fast rotating model shows a peak at low latitudes (between 15° and 40°) followed by a flat region of zero shear at middle latitudes, and larger gradients of Ω at latitudes above 60° (see the red line in Figure 3(f)). Models RC02 and RC03 have profiles that are

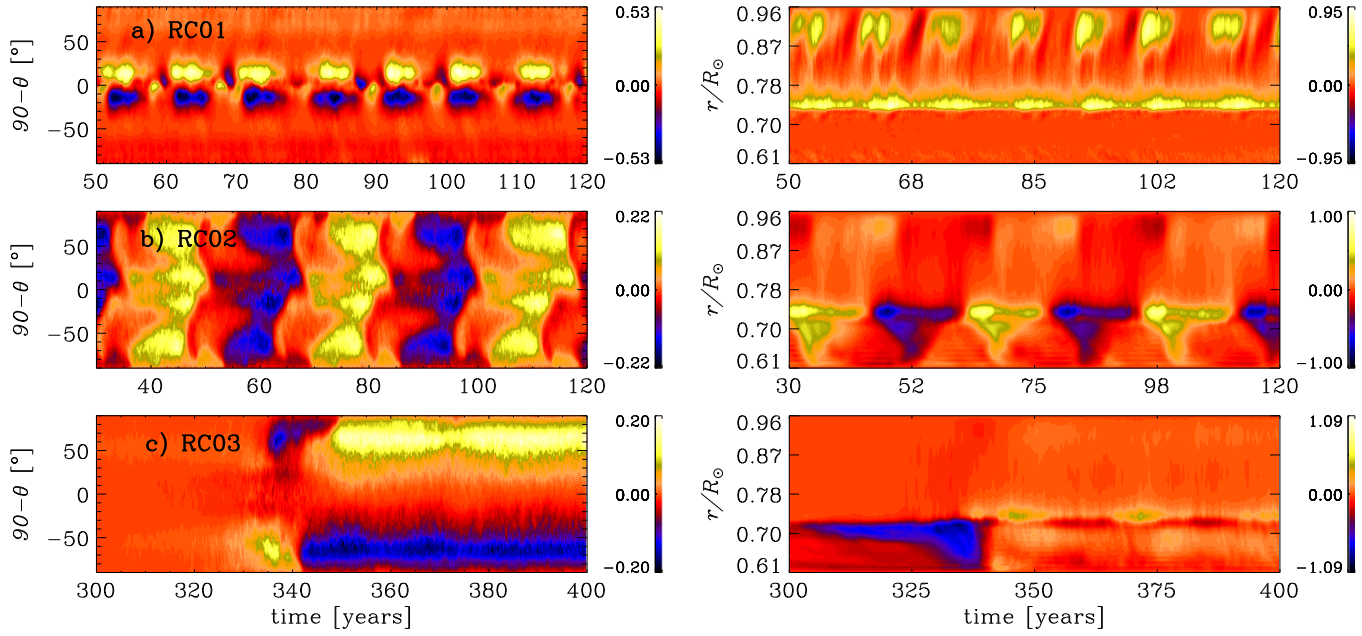

Figure 6. Same as Figure 2 but for the models (a) RC01, (b) RC02, and (c) RC03. The color scales show $\overline{B}_\phi$ in tesla.

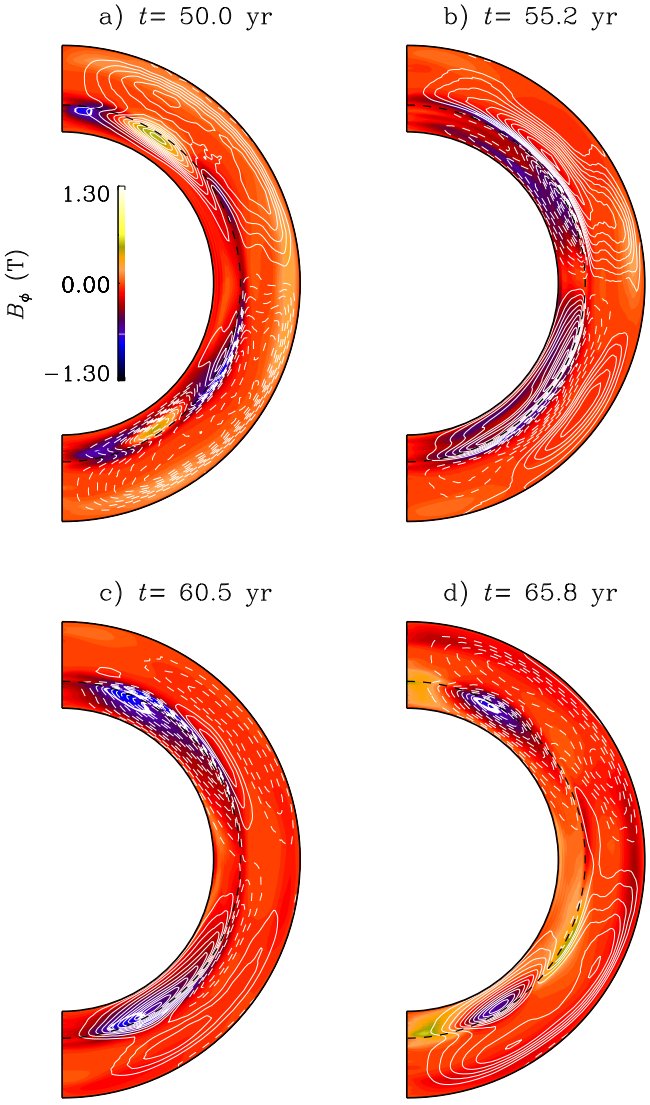

Figure 7. Same as Figure 4 but for model RC02.

comparable at lower and middle latitudes. However, near the poles, the profile of model RC03 shows a stronger latitudinal shear.

The morphology of the steady magnetic field in models RC01 and RC03 can be described in terms of the distribution of its source terms. For model RC01, at the tachocline, both sources of magnetic field are small; the dynamo results in a steady field concentrated at the equator where $\partial_\theta\Omega$ peaks (red dashed line in Figure 3(f)). In this region the α-effect is possibly dominant over the Ω-effect, yet the poloidal component of the field is ∼4 times larger than the toroidal one. In the upper convection zone, $\partial_\theta\Omega$ has larger values at the equator, which explains why the field is concentrated in a band at $\pm 30^\circ$ latitude (Figure 6(a)). The field variations do not lead to polarity reversals, perhaps because the field at the tachocline remains steady. For model RC03 the field reaches its saturation after $t \simeq 340$ yr with steady magnetic fields. Since in this case $\partial_\theta\Omega$ reaches larger values at the poles, the toroidal magnetic field is localized at polar latitudes.

Unlike the oscillatory models without the tachocline, CZ01 and CZ02, the migration of magnetic field in model RC02 with the tachocline cannot be explained solely in terms of the Parker–Yoshimura rule. Because of the long cycle period of activity, other transport processes like the meridional circulation or turbulent pumping can affect the evolution of the magnetic field. At the tachocline the migration of the field can be explained by the Parker–Yoshimura rule (Equation (1)). The field developed at the poles migrates equatorward, and the field developed at the equator migrates poleward. This migrating process can be seen in Figures 7(a)–(d), which, similarly to Figure 4, show half of the dynamo cycle with one magnetic field reversal illustrated in four snapshots. These dynamo waves result from a positive α and negative (positive) values of $\partial_r\Omega$ at higher (lower) latitudes. The upward radial migration from $r \simeq 0.75R_\odot$ to $r \simeq 0.90R_\odot$ is also in agreement with Equation (1) for $\alpha\partial_\theta\Omega > 0$ in this region. In the upper convective layer, above $r \simeq 0.90R_\odot$, there is a region of strong magnetic field, possibly resulting from the large negative radial

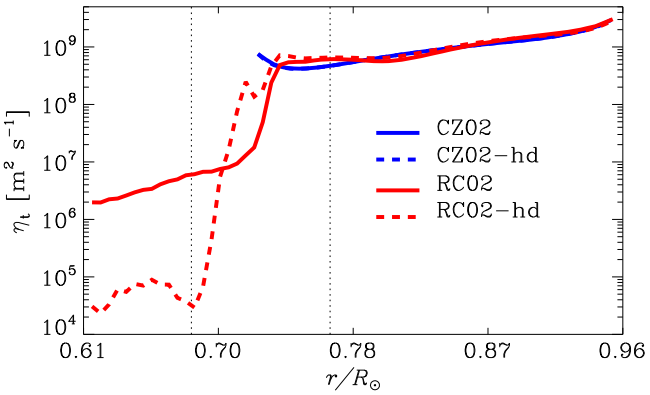

Figure 8. Vertical profiles of the turbulent magnetic diffusivity, η_t, for models CZ02 (blue) and RC02 (red). The dashed lines show the profiles of η_t for the hydrodynamic versions of models CZ02 and RC02.

shear. The latitudinal migration in this region, depicted in Figure 6(b), shows two branches of slight equatorward migration: one branch is located between 0° and ±30° latitude, the other one above 50° latitude. According to Equation (1) these branches would require negative values of $\boldsymbol{s}$; however, this does not agree with the profiles of α and $\partial_r\Omega$ shown in Figures 3(b) and (d) (blue lines). The most equatorial branch of $\overline{B}_\phi$ coincides with a clockwise meridional circulation cell with an equatorward flow at the surface (Figure 5(b)). However, it is impossible to ensure that this is the case, due to the difficulty in disentangling the local and non-local effects contributing to the field migration.

3.3. What Process Governs the Cycle Period?

Perhaps the most interesting difference between the oscillatory dynamo models CZ02 and RC02 is the timescale of the magnetic cycles (i.e., the period of the magnetic polarity reversals). As follows from the mean-field dynamo theory, the magnetic field grows and decays according to the values of the inductive and diffusive terms in the induction equation (Brandenburg & Subramanian 2005). A longstanding problem for mean-field dynamo modelers has been to reconcile the theoretically expected value of the turbulent diffusivity, η_t, with the observed cycle period. In the solar case a mixing-length theory (MLT) estimation of η_t gives values $\sim 10^9$ m^2 s^{-1}, which, in turn, results in dynamo cycles with periods of 2–8 yr (Guerrero et al. 2009) instead of the observed 22 yr. Nonlinearities in the dependence of the turbulent diffusivity on the large-scale magnetic field, like the so-called η-quenching mechanism, have been explored but did not solve the problem (Rüdiger et al. 1994; Guerrero et al. 2009; Muñoz-Jaramillo et al. 2011). The difference in cycle period between the two types of models found in our simulations provides an opportunity to explore this issue.

The radial profile of the turbulent diffusion coefficient, η_t, computed using Equation (9), for both models with the solar rotation rate, CZ02 and RC02, is depicted in Figure 8. From this figure and the values of η_{t0} in Table 2, it can be seen that the profiles and values of η_t in the convection zone match closely in both models. Both cases correspond to a strongly diffusive regime with $\eta_t \simeq 10^9$ m^2 s^{-1} (in agreement with the MLT estimate). However, model CZ02 has a cycle period of ∼2 yr, while model RC02 has a full magnetic cycle period of ∼30 yr. Furthermore, in the same figure, the dashed lines correspond to the turbulent diffusivity of the hydrodynamic versions of the CZ02 and RC02 models. We notice that there is no important diffusivity quenching due to the presence of the saturated magnetic field except for a small fraction of the radius nearby the tachocline where the diffusivity of the magnetic model is smaller (see the region between the vertical dotted lines in Figure 8).

This suggests that the cycle period in model RC02 may be determined by the value of η_t in the region where most of the magnetic field is produced and stored (i.e., at and below the tachocline), which is mainly convectively stable. (Note that η_t does not tend to zero in the radiative layer but to values around $\sim 10^6$ m^2 s^{-1}. This reveals that the magnetic field is inducing turbulent motions in some fraction of the radiative interior.) To verify if this is indeed the case, we have computed the ratio between the diffusion times for models RC02 and CZ02, as follows:

$$\frac{t_d^{\rm RC}}{t_d^{\rm CZ}} \simeq \frac{L_{\rm RC}^2 \langle \eta_t \rangle_{\rm CZ}}{L_{\rm CZ}^2 \langle \eta_t \rangle_{\rm RC}} \simeq 19\,, \qquad (10)$$

where $L_{\rm CZ} = (0.96 - 0.72)\, R_\odot$ is the length scale of the convective layer of model CZ02, and $L_{\rm RC} = (0.77 - 0.68)\, R_\odot$ is the length of the region of model RC02 where most of magnetic field is stored (see vertical dotted lines in Figures 3(a) and (b)); $\langle \eta_t \rangle_{\rm CZ}$ and $\langle \eta_t \rangle_{\rm RC}$ are the radially averaged values of the turbulent diffusivity over the same lengths. Interestingly, this rough estimation agrees fairly well with the ratio between the cycle periods of these two types of models.

It is striking that in model RC02 the magnetic field in the turbulent convection zone, despite the larger local values of η_t, evolves on the same timescale as the magnetic field in the most stable layer with lower diffusivity. If such a non-local mechanism is operating in the Sun, it could explain the 22 yr period of the solar magnetic cycle. This does not necessarily mean, however, that the migration of sunspots observed at the surface is shaped by the meridional circulation at the base of the convection zone as assumed by most of the flux-transport dynamo models. On the contrary, the dynamo in our simulations operates over the entire convection zone, and several processes could influence the generation and migration of magnetic field (e.g., the near-surface rotational shear layer, as argued by Brandenburg 2005; Pipin & Kosovichev 2011).

3.4. Tachocline Instabilities

From Figure 8 it is evident that turbulent motions must be present in the stably stratified layer. Such motions increase the turbulent diffusivity by more than one order of magnitude compared to the pure hydrodynamic model RC02 (red dashed line). The most probable origin of this hydromagnetic turbulence in the stable layer is the development of MHD instabilities at and below the interface between the convective and radiative layers. It has been suggested that these turbulent motions could be significantly helical such that, similarly to the flow in the convection zone, they can result in a kinetic α-effect (e.g., Dikpati & Gilman 2001). The analysis performed in Section 3.2 indicates that the kinetic part of the α-effect in the stable layer is small when compared with its values at the convection zone. Nevertheless, the magnetic contribution to α in the radiative zone is important, as evidenced in Figure 3(b). The development of small-scale helical magnetic structures due to instabilities could explain the existence of this magnetic α-

effect. This, in turn, leads to the generation of large-scale magnetic field (Brandenburg & Subramanian 2005).

This section does not intend to explore in detail the development of all possible tachocline instabilities in the simulations presented here. Such analysis has recently been performed by Lawson et al. (2015) for one of the EULAG-MHD simulations (Passos & Charbonneau 2014). In this section we briefly review the nature of such instabilities, try to identify which of them could be operating in our simulations based on a simple energy analysis, and discuss their contribution to the dynamo mechanism.

Tachocline instabilities have been investigated extensively over the past decades. They can be divided into four distinct kinds according to the energy source (Arlt 2009): (a) shear-driven instabilities; (b) baroclinic instabilities; (c) buoyancy-driven instabilities; and (d) current-driven instabilities. The shear-driven instabilities (e.g., Dziembowski & Kosovichev 1987; Charbonneau et al. 1999; Dikpati & Gilman 2001) are purely hydrodynamic. Due to the latitudinal shear at the tachocline, small perturbations can destabilize the flow given sufficiently strong shear, e.g., more than ∼30% difference between the equator and the pole for a 2D analysis. The 3D stability analysis of Arlt et al. (2005) has shown that the solar tachocline should be nearly stable, in agreement with previous results by Garaud (2001). In the simulations presented in Section 3.2 the difference in the angular velocity between equator and pole is less than 10% for the models RC01 and RC02, and about 30% for the model RC03. It seems unlikely that this kind of instability is developing in these simulations. Baroclinic instabilities (b) are more complex in nature. If the transition region from subadiabatic to superadiabatic is in thermal wind balance, horizontal (azimuthal and latitudinal) perturbation flows can gain some thermal energy and become unstable. Recently Gilman (2015) has demonstrated that the magnetic field has a stabilizing effect on these growing modes. Buoyancy-driven instabilities (c) are presumably responsible for the emergence of magnetic flux tubes. The buoyancy force of low-density parcels of magnetized gas is responsible for their emergence. For toroidal field ropes stored in a stable layer, it is generally true that the magnetic field should surpass the equipartition field strength (see Hughes 2007, and references therein). This is not the case in the simulations above. Strong flux concentration could be achieved in the case of very thin flux tubes, which would require higher grid resolutions. The current-driven instabilities (d) appear whenever there is a large-scale current and their energy source is the large-scale magnetic field. Instabilities of this kind could develop without rotation (e.g., Tayler 1973; Bonanno & Urpin 2012) or with rotation (Pitts & Tayler 1985), or also when the rotation is differential (e.g., Arlt et al. 2005). These latter processes, often called magneto-shear instabilities (Cally et al. 2003), destabilize different configurations of toroidal magnetic bands either by opening the magnetic field lines (the so-called clamshell instability) or by tipping the axis of the magnetic field band. In both cases non-axisymmetric magnetic field is expected to develop out of the axisymmetric field lines. This instability grows for different configurations of toroidal magnetic fields and diminishes the shear. When a latitudinal shear profile and a toroidal field configuration are left to evolve freely, the instability decays after the saturation (Cally et al. 2003). However, if the system is forced, as the solar tachocline should be, both the shear and the magnetic field adjust to a new equilibrium state (e.g., Miesch et al. 2007).

All the ingredients for the onset of the magneto-shear instability are present in the simulations with a radiative zone presented above (RC models). The differential rotation is sustained by the Reynolds stresses and, depending on *Ro*, it induces different configurations of toroidal fields (which in turn react back, readjusting the shear). At some evolutionary stage of the simulation the conditions for the development of the instability are present, creating small-scale flows and magnetic field in the stable layer. As a consequence, a new adjustment should happen until the final steady state of the simulation is achieved.

Following Miesch et al. (2007), we study the time evolution of the different energy sources of the stable layer to verify the existence, and relevance, of such a small-scale, non-axisymmetric, magnetic field. The net energies are computed as follows (Lawson et al. 2015):

$$\begin{aligned}
\mathrm{TME} &= \frac{1}{2\mu_0}\int_{0.61}^{0.7}\int_0^{\pi/2}\int_0^{2\pi} \overline{B}_\phi^2 r^2 \sin\theta d\phi d\theta dr\ ,\\
\mathrm{PME} &= \frac{1}{2\mu_0}\int_{0.61}^{0.7}\int_0^{\pi/2}\int_0^{2\pi} (\overline{B}_r^2 + \overline{B}_\theta^2) r^2 \sin\theta d\phi d\theta dr\ ,\\
\mathrm{NAME} &= \frac{1}{2\mu_0}\int_{0.61}^{0.7}\int_0^{\pi/2}\int_0^{2\pi} \boldsymbol{b}'^2 r^2 \sin\theta d\phi d\theta dr\ ,\\
\mathrm{TKE} &= \frac{1}{2}\int_{0.61}^{0.7}\int_0^{\pi/2}\int_0^{2\pi} \rho\overline{u}_\phi^2 r^2 \sin\theta d\phi d\theta dr\ ,\\
\mathrm{NAKE} &= \frac{1}{2}\int_{0.61}^{0.7}\int_0^{\pi/2}\int_0^{2\pi} \rho\boldsymbol{u}'^2 r^2 \sin\theta d\phi d\theta dr,
\end{aligned} \tag{11}$$

where TME, PME, and TKE are the axisymmetric toroidal and poloidal magnetic energies and the azimuthal kinetic energy, respectively. NAME and NAKE stand for non-axisymmetric magnetic and kinetic energies. The resulting evolution profiles are presented in Figure 9. The axisymmetric toroidal (poloidal) magnetic and kinetic energies are depicted by the continuous black (green) and red lines; the non-axisymmetric magnetic and kinetic energies are shown by the dashed blue and orange lines. The results indicate that all models develop non-axisymmetric motions and magnetic field in the stable layer, but the energy distribution is different from model to model. Models RC01 and RC02 reach a steady state after a few years of evolution. In the first case the toroidal magnetic field is weak and erratic in the radiative layer (see right panel of Figures 6(a) and 9(a)). The weakness of this component of the field in the stable layer probably results from the inhibition of penetrative convection by the fast rotation. The poloidal field has larger energy, which is consistent with the presence of a non-zero α-effect in this region (red line in Figure 3(b)).

The case of model RC02 is more interesting since there is an important mean oscillatory toroidal field. The non-axisymmetric magnetic field is also oscillatory and exhibits a phase lag with respect to the toroidal field (see the vertical dashed lines indicating particular peak times for TME and NAME). This behavior is similar to that obtained by Miesch et al. (2007) and Lawson et al. (2015), who observe the growth and decay of these quantities. Nonetheless, in these works the values of NAME and TME are similar to each other and the phase lag is

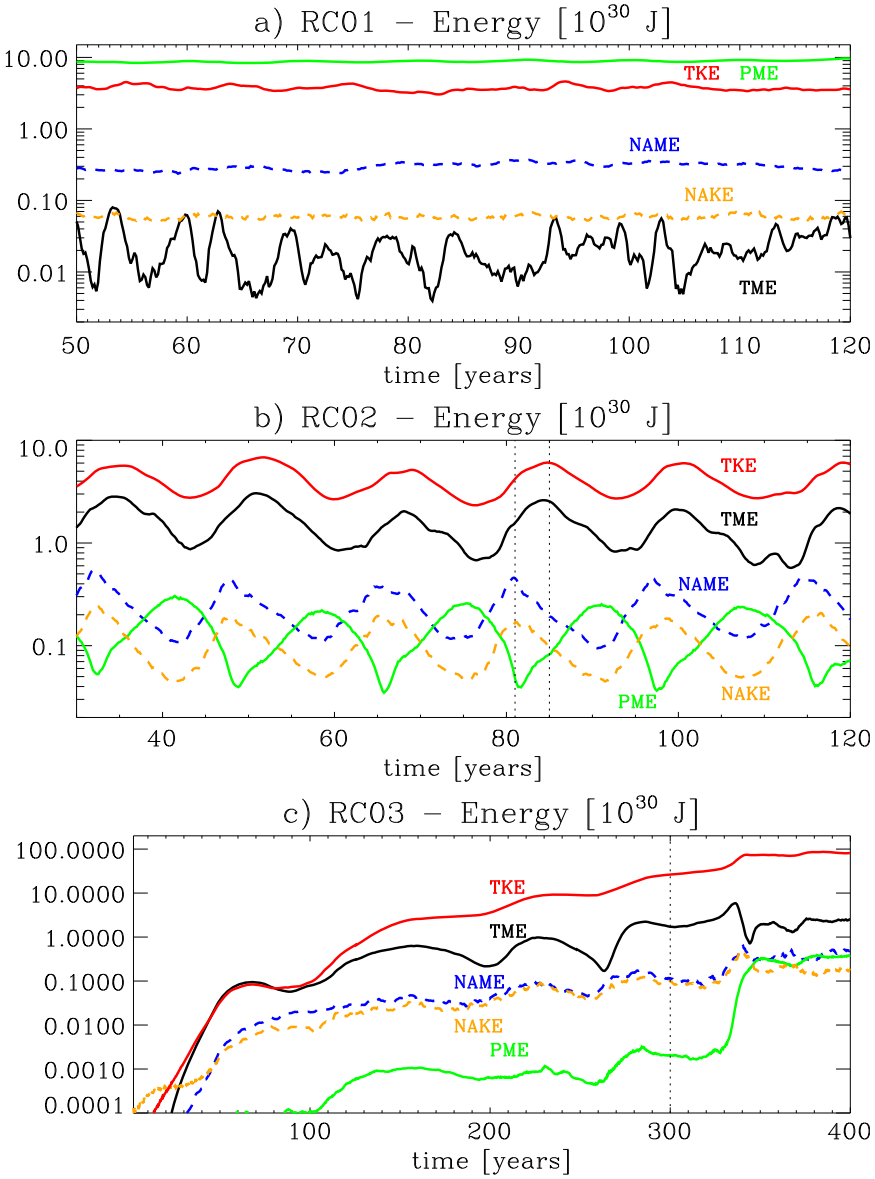

Figure 9. Volume integral of the different energies in the stable region for the models (a) RC01, (b) RC02, and (c) RC03). The toroidal magnetic energy (TME) is shown in black, the toroidal kinetic energy (TKE) in red, the poloidal field energy (PFE) in green, the non-axisymmetric magnetic field (NAMF) with the dashed blue line, and the non-axysymmetric kinetic energy (NAKE) with the dashed orange line. The dotted lines in the middle panels highlight the phase lag between the axisymmetric and the non-axisymmetric quantities. In the bottom panel, the dotted line shows the point from which the butterfly diagram of Figure 6(c) was plotted.

about $\pi/2$. In the model RC02 the toroidal energy is larger than the turbulent magnetic energy. It is noteworthy that the mean poloidal field oscillates with a $\pi/2$ phase lag with respect to the non-axisymmetric magnetic field (i.e., when the PME grows the NAME decays). Note also that the PME is smaller than the NAME, which is suggestive of a magnetic α-effect giving rise to a large-scale poloidal magnetic field. The energy of the turbulent motions oscillates with the same phase as the turbulent field but with lower amplitude. Finally, note also that the mean kinetic energy is larger than the toroidal energy; the figure indicates acceleration and deceleration of the angular velocity in phase with the toroidal magnetic field (G. Guerrero et al. 2016, in preparation).

The model RC03 is the one that takes longer to reach a steady state. Since this case is the one that exhibits more variation, in Figure 9(c) we present the entire evolution of the energies in the stable layer. The figure shows that the small-scale non-axisymmetric components of the kinetic and magnetic field energy develop after the development of the toroidal field and that the evolution of these two quantities is closely linked (see dashed lines). The mean toroidal kinetic energy evolves together with the mean toroidal field. When the non-axisymmetric modes develop, the toroidal kinetic energy grows. We interpret this behavior as the inward transport of angular momentum, which causes the stable region to accelerate. The poloidal magnetic energy also develops after the establishment of MHD turbulence in the radiative zone. After around 350 years of evolution the rotation seems to achieve a steady state. This modifies all the other quantities, especially the mean poloidal energy, which grows by about two orders of magnitude in a few years. Note that the α-effect has important positive values in the entire

stable layer (see the profile of α for the model RC03, the green line in Figure 3(b), which was computed in the final phase of the evolution).

In general, it is evident that the dynamics of the convectively stable stratified layer increases in complexity for models with larger *Ro*. This, of course, means a dependence on the unstable region where phenomena like penetrative convection or turbulent pumping are established. The non-axisymmetric flow and field seem to be contributing to the generation of poloidal field. From the FOSA analyses presented above, it is the small-scale magnetic field that is contributing through the magnetic α-effect. The turbulent flows in the radiative zone increase the turbulent diffusion in this region. For the oscillatory model RC02, it defines the cycle period of the large-scale magnetic field in the entire domain.

4. SUMMARY AND CONCLUSIONS

We have performed global 3D MHD simulations of turbulent convection in rotating spherical shells using the anelastic approximation. We have used the code EULAG-MHD, which captures the contribution of the unresolved scales via an implicit SGS model. The main goal of this work was the comparison of the properties of global dynamos for models of the convective envelope only (CZ models), and models that include a part of the radiative core below the convection zone (RC models). The stratification is set in such a way that *Ro* is roughly the same in corresponding CZ and RC models. These simulations aimed at contributing to a broader understanding of the amplification and dynamics of large-scale magnetic fields in the Sun and solar-type stars. Our main conclusions are summarized and briefly discussed below.

The resulting differential rotation profile depends on the balance between the Coriolis, buoyancy, and Lorentz forces. All the cases presented here develop a solar-like differential rotation (with faster rotation at the equator and slower rotation at the poles). This result differs from the purely hydrodynamic simulations for which the antisolar rotation type is found as a robust feature of slowly rotating convection (Gilman 1976; Glatzmaier & Gilman 1982; Steffen & Freytag 2007; Käpylä et al. 2011; Matt et al. 2011; Guerrero et al. 2013; Gastine et al. 2014).

Nevertheless, our results are in agreement with recent global models that obtain the transition from antisolar to solar-like rotation due to the presence of dynamo-generated magnetic fields (Fan & Fang 2014; Simitev et al. 2015). Also, Karak et al. (2015) have studied the dynamo action over a broad range of *Ro* and found an antisolar rotation pattern in slowly rotating stars. In our simulations, the slowest rotating models with $\Omega = \Omega_\odot/2$, CZ03 and RC03, develop a large-scale magnetic field whose energy is several orders of magnitude smaller than the kinetic energy. We did not obtain a regime in which the rotation pattern switches from solar to antisolar.

The models without a tachocline develop substantial latitudinal differential rotation. Tilted, conical, iso-rotation contours are obtained for the models with relatively slower rotation (i.e., models CZ02 and CZ03). The results reproduce remarkably well the differential rotation in the solar convection zone, with the equator-to-60° latitude difference, $\chi_\Omega \sim 0.18$ (the same as in the Sun), and also reproduce the NSSL.

Because of the highly subadiabatic stable region, the simulations including the upper part of the radiative interior develop a tachocline, i.e., a rotational shear layer between the radiative and convective zones. The model with faster rotation ($\Omega = 2\Omega_\odot$), RC01, does not develop a NSSL. The more slowly rotating models, which have a larger influence of the buoyancy force, RC02 ($\Omega = \Omega_\odot$) and RC03 ($\Omega = \Omega_\odot/2$), do develop a NSSL.

The meridional circulation in the models with a radiative zone shows a poleward flow at latitudes >30° and a multicellular pattern radially distributed. This last characteristic resembles and theoretically supports recent helioseismology results. It is noteworthy, however, that to date no global simulation has been able to accurately reproduce both the solar differential rotation and the meridional circulation. The computational difficulties in simulating the processes in the upper part of the convection zone are perhaps the reason for the general lack of success.

Large-scale dynamo action is observed in all models. The differential rotation, dynamo growth rate, and magnetic field topology depend on *Ro*. The dynamo solutions include both steady and oscillatory dynamo regimes. The ratio between the magnetic and kinetic energies increases with the rotation rate, i.e., the smaller *Ro* the larger e_M/e_K (see Table 1). Our results partially agree with those of Petit et al. (2008) since we observe a linear dependence of the mean magnetic energy on the rotation rate. Furthermore, in the fast rotating model with the tachocline, RC01, the magnetic energy is deposited in the poloidal magnetic field. Although most of this poloidal field is concentrated at the tachocline, this is reminiscent of the magnetic structure of fast rotating young stars, whose observations indicate strong poloidal fields (Gregory et al. 2012).

Using our simulations, we have computed the inductive and dissipative terms of the mean-field induction equation. We notice first that in both sets of dynamo models, the inductive term due to the radial shear is inversely proportional to the rotation rate. The shear is localized mainly in the boundary layers, i.e., the interface between the radiative and convective zones, and in the upper surface. On the other hand, the inductive term due to the latitudinal shear in the simulations without the tachocline is proportional to Ω_0. In the models RC01, RC02, and RC03, when the rotation is fast, $\partial_\theta\Omega$ peaks at the equator (RC01). When the rotation is slow, $\partial_\theta\Omega$ peaks at the poles (RC03).

The turbulent coefficients η_t and α were computed using the FOSA approximation. We observe no dependence of the kinetic counterpart of α, α_k, on *Ro*. However, the magnetic counterpart α_m (Equations (6) and (7)) clearly anticorrelates with *Ro*, i.e., the smaller *Ro*, the larger the magnetic field and, thus, the larger the small-scale current helicity. Consequently, the magnetic α-effect, computed here via the current helicity, could work as an inductive term in the generation of magnetic fields. This partially agrees with the results of Vishniac & Shapovalov (2014) in the sense that both kinetic and magnetic parts of the α-effect may act as a source of magnetic field.

In the oscillatory dynamo models without tachocline, CZ01 and CZ02, the evolution of the field is consistent with dynamo waves propagating according to the Parker–Yoshimura sign rule. This is not the case, however, for the tachocline model RC02, in which the migration of the field can be explained by this rule only in some regions. Because the evolution of the field in this model is slow (on a timescale of ~30 years), other factors like the meridional circulation and/or turbulent magnetic pumping, could be influencing the field transport.

Though the FOSA is the simplest form of computing the mean-field coefficients, in general terms our 3D simulation results give support to the mean-field dynamo theory as a formalism to explain solar and stellar dynamos. A more sophisticated technique, such as the test-field method (e.g., Schrinner et al. 2005; Brandenburg et al. 2008), could provide a better inference of these coefficients and thus allow a better analysis.

The cycle period for the models without tachocline, CZ01 and CZ03, is short (about two years) compared to the solar cycle. In the slow and fast rotating tachocline models, RC01 and RC03, the dynamo regimes are stationary. However, in the model RC02, with the solar rotation rate and the tachocline, the field is oscillatory with a period of about 30 years. This timescale is comparable with the solar cycle; however, unlike in the Sun, the toroidal magnetic field is symmetric across the equator.

In the RC models, a strong toroidal magnetic field generated by the dynamo is concentrated at or below the interface between the convective and radiative layers. This indicates that the main source of the magnetic field is the radial shear at the tachocline. This effect has enormous influence on the general evolution of the models. First, this strong magnetic field modifies the mean-flow profiles via the Maxwell stresses; and second, because the field is deposited in a convectively stable region, its evolution occurs on longer timescales than in the models without the tachocline. Despite the field production being distributed over the simulation domain, the dynamo period is regulated by the diffusion time of the toroidal magnetic field in the deeper, more stable layers. The deep seated magnetic field seems to control the evolution of the magnetic field in the rest of the convection zone. This result could explain a longstanding problem in mean-field modeling, i.e., the coexistence of a highly turbulent magnetic diffusivity, of the order of $10^9\,\mathrm{m^2\,s^{-1}}$, and the 22 yr cycle period of the Sun.

The value of the magnetic diffusivity, and so of the diffusion time, in the stable layer is a product of the small-scale motions generated by MHD instabilities. We have studied the temporal evolution of the mean axisymmetric, as well as the non-axisymmetric, kinetic and magnetic energy components. This temporal evolution suggests that once the toroidal field is established due to the strong radial shear, magneto-shear instabilities develop in the radiative zone, generating turbulent motions and magnetic fields. The results support the idea of a magnetic α-effect as a source of poloidal field. The turbulent motions, on the other hand, enhance the magnetic diffusivity. Therefore, the system adjusts itself to the new quantities until a new steady state is reached. The dynamics in the stable layer depends on *Ro*: slowly rotating models exhibit more complex behavior and take longer to achieve a steady state. In model RC02 the turbulent motions in the stable layer define the ∼30 yr cycle period. The solar model with the tachocline of Ghizaru et al. (2010) uses a stratification that results in slower convective, less penetrative, motions. For that reason the cycle period is longer that the one found here. The difference in the cycle period between models with and without tachocline, as well as the development of a magnetic α-effect, suggest that the instabilities in the tachocline might be of significant importance in the solar dynamo.

One could ask why RC models do not exhibit the same short-period dynamo that is observed in the CZ models due to the latitudinal shear alone. The answer lies in the backreaction of the magnetic field on the fluid dynamics via the Lorentz force. This influence can be easily noticed by comparing the profiles of Ω between the models CZ02 and RC02. In numerical experiments, not presented here, we have verified that the strength of the toroidal magnetic field (and thus its influence on the flow) at the tachocline can be controlled by varying different model ingredients. The radial shear source term is particularly sensitive to the ambient state profile, Θ_e. For instance, changes in parameters such as the thickness of the transition between radiative and convective zones, the amplitude of the thermal oscillations, or the adiabaticity of radiative and convective layers could result in different rotation and dynamo patterns. The solar values of these parameters are not fully established. We should also stress that a better understanding of the effects of the turbulent diffusion—in particular, the feedback of the magnetic field upon this diffusion—is still necessary (e.g., de Gouveia Dal Pino et al. 2012; Karak et al. 2014; R. Santos-Lima 2015, in preparation).

We conclude that tachoclines play an important role in solar and stellar dynamos. Modelers should be careful when interpreting results obtained in simulations that do not include this rotational shear layer. From this work, several new studies seem to be promising for the understanding of the solar/stellar rotation and magnetism. For instance, a study of mean flows and angular momentum balance for cool stars in the presence of magnetic fields could help us to understand the cyclic and non-cyclic stellar activity. Models without a tachocline, which evolve on short timescales and could be interpreted more easily, could help in the study of the origin of stochasticity and intermittency in turbulent flows. This will provide new insights into the physical origin of Maunder-like solar minima. The results are also encouraging for the study of the evolution of rotation and magnetism in young stars.

We thank the anonymous referee for comments and suggestions on the manuscript. This work was partly funded by FAPESP grants 2013/11679-4 (G.G.) and 2013/10559-5 (E.M.G.D.P.), CNPq grant 306598/2009-4 (E.M.G.D.P.), and NASA grants NNX09AJ85g and NNX14AB70G. G.G. also thanks CNPq for travel support. P.K.S. is supported by funding received from the European Research Council under the European Union's Seventh Framework Programme (FP7/2012/ERC Grant agreement no. 320375). The simulations were performed in the NASA cluster Pleiades and the computing facilities of the Laboratory of Astroinformatics (IAG/USP, NAT/Unicsul) supported by a FAPESP (grant 2009/54006-4).

REFERENCES

Arlt, R. 2009, in ASP Conf. Ser. 416, Solar-Stellar Dynamos as Revealed by Helio- and Asteroseismology: GONG 2008/SOHO 21, ed. M. Dikpati et al. (San Francisco, CA: ASP), 467
Arlt, R., Sule, A., & Rüdiger, G. 2005, A&A, 441, 1171
Augustson, K., Brun, A. S., Miesch, M., & Toomre, J. 2015, ApJ, 809, 149
Augustson, K. C., Brun, A. S., & Toomre, J. 2013, ApJ, 777, 153
Baliunas, S. L., Donahue, R. A., Soon, W. H., et al. 1995, ApJ, 438, 269
Bonanno, A. 2013, SoPh, 287, 185
Bonanno, A., & Urpin, V. 2012, ApJ, 747, 137
Brandenburg, A. 2005, ApJ, 625, 539
Brandenburg, A., Rädler, K.-H., Rheinhardt, M., & Subramanian, K. 2008, ApJL, 687, L49
Brandenburg, A., & Subramanian, K. 2005, PhR, 417, 1

Brown, B. P., Browning, M. K., Brun, A. S., Miesch, M. S., & Toomre, J. 2010, ApJ, 711, 424
Browning, M. K., Miesch, M. S., Brun, A. S., & Toomre, J. 2006, ApJL, 648, L157
Brun, A. S., Miesch, M. S., & Toomre, J. 2004, ApJ, 614, 1073
Cally, P. S., Dikpati, M., & Gilman, P. A. 2003, ApJ, 582, 1190
Charbonneau, P. 2010, LRSP, 7, 3
Charbonneau, P., Dikpati, M., & Gilman, P. A. 1999, ApJ, 526, 523
Chatterjee, P., Nandy, D., & Choudhuri, A. R. 2004, A&A, 427, 1019
Cossette, J.-F. 2015, PhD thesis, Université de Montreal
Covas, E., Moss, D., & Tavakol, R. 2004, A&A, 416, 775
de Gouveia Dal Pino, E. M., Leão, M. R. M., Santos-Lima, R., et al. 2012, PhyS, 86, 018401
Dikpati, M., & Gilman, P. A. 2001, ApJ, 559, 428
Domaradzki, J. A., Xiao, Z., & Smolarkiewicz, P. K. 2003, PhFl, 15, 3890
Dziembowski, W., & Kosovichev, A. 1987, AcA, 37, 341
Elliott, J. R., & Smolarkiewicz, P. K. 2002, IJNMF, 39, 855
Fan, Y., & Fang, F. 2014, ApJ, 789, 35
Featherstone, N. A., & Miesch, M. S. 2015, ApJ, 804, 67
Garaud, P. 2001, MNRAS, 324, 68
Gastine, T., Yadav, R. K., Morin, J., Reiners, A., & Wicht, J. 2014, MNRAS, 438, L76
Ghizaru, M., Charbonneau, P., & Smolarkiewicz, P. K. 2010, ApJL, 715, L133
Gilman, P. A. 1976, in IAU Symp. 71, Basic Mechanisms of Solar Activity, ed. V. Bumba, & J. Kleczek (Dordrecht: Reidel), 207
Gilman, P. A. 2015, ApJ, 801, 22
Glatzmaier, G. A., & Gilman, P. A. 1982, ApJ, 256, 316
Gregory, S. G., Donati, J.-F., Morin, J., et al. 2012, ApJ, 755, 97
Guerrero, G., Chatterjee, P., & Brandenburg, A. 2010, MNRAS, 409, 1619
Guerrero, G., & de Gouveia Dal Pino, E. M. 2008, A&A, 485, 267
Guerrero, G., Dikpati, M., & Deeepak, E. M. 2009, ApJ, 701, 725
Guerrero, G., Smolarkiewicz, P. K., Kosovichev, A. G., & Mansour, N. N. 2013, ApJ, 779, 176
Hathaway, D. H. 2012, ApJ, 760, 84
Hotta, H., Rempel, M., & Yokoyama, T. 2015, ApJ, 798, 51
Hughes, D. W. 2007, in The Solar Tachocline, ed. D. W. Hughes, R. Rosner, & N. O. Weiss (Cambridge: Cambridge Univ. Press), 275
Jouve, L., Brown, B. P., & Brun, A. S. 2010, A&A, 509, A32
Käpylä, P. J., Mantere, M. J., & Brandenburg, A. 2012, ApJL, 755, L22
Käpylä, P. J., Mantere, M. J., Guerrero, G., Brandenburg, A., & Chatterjee, P. 2011, A&A, 531, A162
Karak, B. B., Käpylä, P. J., Käpylä, M. J., et al. 2015, A&A, 576, A26
Karak, B. B., Rheinhardt, M., Brandenburg, A., Käpylä, P. J., & Käpylä, M. J. 2014, ApJ, 795, 16
Lawson, N., Strugarek, A., & Charbonneau, P. 2015, ApJ, 813, 95
Lipps, F. B., & Hemler, R. S. 1982, JAtS, 39, 2192
Margolin, L. G., Smolarkiewicz, P. K., & Wyszogradzki, A. A. 2006, ATJAM, 73, 469
Masada, Y., Yamada, K., & Kageyama, A. 2013, ApJ, 778, 11
Matt, S. P., Do Cao, O., Brown, B. P., & Brun, A. S. 2011, AN, 332, 897
Miesch, M. S., Gilman, P. A., & Dikpati, M. 2007, ApJS, 168, 337
Miesch, M. S., & Hindman, B. W. 2011, ApJ, 743, 79
Mitra, D., Moss, D., Tavakol, R., & Brandenburg, A. 2011, A&A, 526, A138
Muñoz-Jaramillo, A., Nandy, D., & Martens, P. C. H. 2011, ApJL, 727, L23
Parker, E. N. 1955, ApJ, 122, 293
Passos, D., & Charbonneau, P. 2014, A&A, 568, A113
Petit, P., Dintrans, B., Solanki, S. K., et al. 2008, MNRAS, 388, 80
Pipin, V. V. 2015, MNRAS, 451, 1528
Pipin, V. V., & Kosovichev, A. G. 2011, ApJ, 741, 1
Pipin, V. V., & Kosovichev, A. G. 2013, ApJ, 776, 36
Pitts, E., & Tayler, R. J. 1985, MNRAS, 216, 139
Pouquet, A., Frisch, U., & Leorat, J. 1976, JFM, 77, 321
Prusa, J. M., Smolarkiewicz, P. K., & Wyszogrodzki, A. A. 2008, CF, 37, 1193
Racine, É, Charbonneau, P., Ghizaru, M., Bouchat, A., & Smolarkiewicz, P. K. 2011, ApJ, 735, 46
Rüdiger, G., Kitchatinov, L. L., Küker, M., & Schultz, M. 1994, GApFD, 78, 247
Schad, A., Timmer, J., & Roth, M. 2013, ApJL, 778, L38
Schou, J., Antia, H. M., Basu, S., et al. 1998, ApJ, 505, 390
Schrinner, M., Rädler, K.-H., Schmitt, D., Rheinhardt, M., & Christensen, U. 2005, AN, 326, 245
Simitev, R. D., Kosovichev, A. G., & Busse, F. H. 2015, ApJ, 810, 80
Smolarkiewicz, P. K. 2006, IJNMF, 50, 1123
Smolarkiewicz, P. K., & Charbonneau, P. 2013, JCoPh, 236, 608
Smolarkiewicz, P. K., & Margolin, L. G. 2007, Implicit Large Eddy Simulations: Computing Turbulent Fluid Dynamics (Cambridge: Cambridge Univ. Press), 413
Steffen, M., & Freytag, B. 2007, AN, 328, 1054
Sur, S., Shukurov, A., & Subramanian, K. 2007, MNRAS, 377, 874
Tayler, R. J. 1973, MNRAS, 161, 365
Ulrich, R. K. 2010, ApJ, 725, 658
Vishniac, E. T., & Shapovalov, D. 2014, ApJ, 780, 144
Warnecke, J., Käpylä, P. J., Käpylä, M. J., & Brandenburg, A. 2014, ApJL, 796, L12
Yoshimura, H. 1975, ApJ, 201, 740
Zhao, J., Bogart, R. S., Kosovichev, A. G., Duvall, T. L., Jr., & Hartlep, T. 2013, ApJL, 774, L29